TAMPERE UNIVERSITY OF TECHNOLOGY

OSKARI LAAKSONEN

EVALUATION OF LESION SEGMENTATION METHODS IN PEPTIDE RECEPTOR RADIONUCLIDE THERAPY

Master of Science Thesis

Examiners:
Professor Hannu Eskola and
Adjunct Professor Antti Sohlberg
Examiners and topic approved in
the faculty of Computing and
Electrical Engineering on
8th October, 2014

ABSTRACT

TAMPERE UNIVERSITY OF TECHNOLOGY
Master's Degree Programme in Signal Processing and Communications Engineering
LAAKSONEN, OSKARI: Evaluation of lesion segmentation methods in peptide receptor radionuclide therapy
Master of Science Thesis, 47 pages, 4 appendix pages
October 2014
Major: Biomedical Engineering
Examiners: Professor Hannu Eskola and Adjunct Professor Antti Sohlberg
Superivisors: Licentiate of Philosophy Eero Hippeläinen
Keywords: Peptide receptor radionuclide therapy, SPECT, dosimetry, ^{177}Lu-dotatate, segmentation, lesion

Gastroenteropancreatic neuroendocrine tumors (GEP-NETs) are a group of tumours, which originate from the neuroendocrine system. GEP-NETs are characterized by overexpression of somatostatin receptors and can therefore be targeted using radiolabelled somatostatin analogues for peptide receptor radionuclide therapy (PRRT). The Lutetium-177 labelled somatostatin analogs DOTA-TOC and DOTA-TATE are being increasingly used for PRRT. The radioactive Lutetium-177 destroys tumor cells by emitting ionizing radiation. Unfortunately, also normal healthy organs express somatostatin receptors and thus the PRRT can cause significant radiation load to normal tissue. In order to protect the healthy organs and to maximize the radiation dose of the tumors radionuclide therapies need to be planned well by doing individual dosimetry.

Tumor dosimetry requires segmentation of the tumors from the background. Conventionally this segmentation has been performed manually, but the manual segmentation is often very dependent on skills of the operator who is doing the segmentation and it might not be very reproducible. These problems can be avoided with the use of automatic segmentation methods. Even though automatic segmentation has lately been a hot topic in positron emission tomography (PET) these methods have not been studied in PRRT.

In this Master of Science thesis automatic segmentation methods were studied from the PRRT perspective. Four segmentation methods were chosen to be evaluated: thresholding, k-means clustering, fuzzy-c-means clustering and expectation maximization. The evaluation was performed using simulated and real clinical single photon emission computed tomography (SPECT) images acquired during PRRT. The segmentation methods were compared with the help of Dice similarity coefficient (DSC), Classification error (CE) and the integral of the time activity curve.

The results state that expectation maximization is the most accurate algorithm of the four tested methods. It maximizes DSC and minimizes CE with every phantom. Thresholding gave promising results, but the optimal thresholding values had to be sought for each phantom, which made the method time-consuming. K-means clustering and fuzzy-c-means clustering were less successful. The accuracy of the methods with patient data is hard to estimate, due to the lack of the ground truth. However, the results with the patient data are very similar to the results obtained with the phantom data and they showed that segmentation has a big impact on the calculated tumor dose.

TIIVISTELMÄ

TAMPEREEN TEKNILLINEN YLIOPISTO
Signaalinkäsittelyn ja tietoliikennetekniikan koulutusohjelma
LAAKSONEN, OSKARI: Kasvainsegmentointimenetelmien arviointi peptidireseptoriradionuklidihoidoissa
Diplomityö: 47 sivua, 4 liitesivua
Lokakuu 2014
Pääaine: Lääketieteellinen tekniikka
Tarkastajat: Professori Hannu Eskola, dosentti Antti Sohlberg
Ohjaaja: filosofian lisensiaatti Eero Hippeläinen
Avainsanat: Peptidireseptoriradionuklidihoito, SPECT, annoslaskenta, ^{177}Lu-dotatate, segmentointi, kasvain

Gastroenteropankreaaliset neuroendokriiniset kasvaimet ovat lähtöisin neuroendokriinisestä järjestelmästä. Kasvaimet ylituottavat somatostatiinireseptoreita, mistä johtuen ne voidaan kohdentaa peptidireseptoriradionuklidihoidoissa (PRRT) käyttäen radioleimattuja somatostatiinianalogeja. Lutetium-177 leimattujen somatostatiinianalogien DOTA-TOC ja DOTA-TATE käyttö PRRT:ssa on lisääntynyt. Radioaktiivinen lutetium-177 tuhoaa kasvainsoluja emittoimalla ionisoivaa säteilyä. Valitettavasti myös terveet kudokset sisältävät somatostatiinireseptoreja. Siitä johtuen peptidireseptoriradionuklidihoidot voivat aiheuttaa merkittävää säteilykuormitusta terveisiin kudoksiin. Jotta terveitä kudoksia pystyttäisiin suojaamaan ja kasvaimiin kohdistuvaa säteilyannosta maksimoimaan, radionuklidihoidot täytyy suunnitella tarkasti käyttäen yksilöllistä annoslaskentaa.

Kasvaindosimetrian onnistuminen vaatii kasvainten segmentoimista taustasta. Tavanomaisesti segmentointi suoritetaan käsin, mutta manuaalisegmentointi on usein erittäin riippuvainen käyttäjän taidoista, eikä ole toistettavissa. Ongelmat voidaan välttää automaattisten segmentointimenetelmien avulla. Vaikka automaattinen segmentointi on suosittu tutkimuskohde positroniemissiokuvantamisessa (PET), ei menetelmiä ole tutkittu PRRT:ssa.

Tässä diplomityössä on tutkittu automaattisia segmentointimenetelmiä peptidireseptoriradionuklidihoitojen näkökulmasta. Työhön on valittu neljä segmentointimenetelmää: kynnystäminen (thresholding), k-means klusterointi, fuzzy-c-means klusterointi ja todennäköisyyden maksimointi (expectation maximization). Menetelmien arviointi on suoritettu käyttäen peptidireseptoriradionuklidihoidoista saatuja rekonstruoituja SPECT kuvia. Työn toteutuksessa on käytetty sekä fantomi- että potilasdataa. Segmentointimenetelmiä vertailtiin käyttäen apuna Dice similarity coefficient (DSC) ja Classification error (CE) -menetelmiä.

Tulosten mukaan expectation maximization on tarkin neljästä segmentointimenetelmästä. Se maksimoi DSC:n ja minimoi CE:n. Myös eri arvoilla testattu thresholding onnistui segmentoinnissa hyvin, mutta optimaaliset arvot täytyi etsiä, ja menetelmä osoittautui aikaa vieväksi. K-means klusterointi sekä fuzzy-c-means klusterointi eivät olleet tarkkoja. Potilasdatatuloksien tarkkuutta on vaikea arvioida, koska referenssidata puuttuu. Tulokset ovat kuitenkin samankaltaisia kuin fantomidatan kanssa saadut tulokset ja ne osoittavat että segmentointimenetelmän valinnalla on iso vaikutus tuumorin absorboituneeseen annokseen.

PREFACE

This Master of Science thesis is made at Tampere University of Technology, in the department of Biomedical Engineering. This thesis was made in co-operation with Eero Hippeläinen and Antti Sohlberg, since this is a part of the doctoral thesis of Eero Hippeläinen.

I would like to thank my examiner, Professor Hannu Eskola, for offering me this interesting topic for my thesis. I want to express my sincere gratitude to my other examiner, Antti Sohlberg, and my supervisor, Eero Hippeläinen. Without them I would have not succeeded with my thesis. I would also like to wish good luck to Eero with his dissertation project.

Finally, I would like to thank from all my heart my beloved Susanna for encouraging me during the thesis project, and my parents and brother who have always supported and believed in me during my life.

Tampere, 17th October 2014

Oskari Laaksonen

TABLE OF CONTENTS

LIST OF SYMBOLS

A	activity
A	atomic mass
$A(r_S, t)$	activity for each source organ (r_S) at time (t)
$\tilde{A}(r_S, T_D)$	time-integrated activity in source organ during the specified dose integration period T_D
c_k	kth class cluster center
D	absorbed dose
$D_{T,R}$	absorbed dose in tissue T by radiation type R
$D(r_T, T_D)$	mean dose to a target organ
E	effective dose
E_i	mean energy of a given radiation emission
e^-	electron
f(x,y)	intensity value of a pixel
f(x)	value function with argument x
g(x,y)	modified intensity value of a pixel
H_T	equivalent dose absorbed by tissue T
$H_{T,R}$	equivalent dose in tissue T by radiation type R
$J(x, c)$	objective function of k-means clustering
K	number of tissue classes
$L(\pi, \mu, \sigma)$	likelihood
$M(r_T, t)$	target organ mass at time t
m	mass
N	total number of radioactive atoms
N	number of voxels
${}^{A}_{Z}N$	parent nuclide
${}_{Z+1}{}^{A}N$	daughter nuclide
p_{ik}	maximum likelihood estimation of an unknown parameter
R	radiation type

r_S	source organ
S	S factor
t	time
T	tissue
T	threshold value
T_D	specified dose integration period
ν_e	antineutrino
w_R	radiation weigting factor
w_T	corresponding weighting factor
x	x coordinate
x_i	feature vector at the ith location
y	y coordinate
Y_i	yield
Z	atomic number
ε	mean energy
π	mixing parameter
μ	Gaussian parameter
σ	Gaussian parameter
$\phi(r_T \leftarrow r_S, E_i, t)$	absorbed fraction

TERMS AND ABBREVIATIONS

2D	Two-dimensional
3D	Three-dimensional
4D	Four-dimensional
AUC	Area under the curve
CE	Classification error
CT	Computed tomography
DOTA	1,4,7,10-tetraazacyclododecane-1,4,7,10-tetraacetic acid
DSC	Dice similarity coefficient
E-step	Expectation step
EM	Expectation maximization
FCM	Fuzzy c-means clustering
GEP-NET	Gastroenteropancreatic neuroendocrine tumor
HDR	High dose rate
^{131}I	Iodide-131
ICRP	International Commission on Radiological Protection
^{111}In	Indium-111
KM	K-means clustering
LDR	Low dose rate
^{177}Lu	Lutetium-177
M-step	Maximization step
MC	Monte Carlo
MCAT	Mathematical cardiac torso
MIRD	Medical Internal Radiation Dose
ML	Maximum Likelihood
MRI	Magnetic resonance imaging
NCAT	Non-uniform rational B-spline -based cardiac torso
NCE	Negative classification error
NET	Neuroendocrine tumor

NURBS	Non-uniform rational B-spline
OS-EM	Ordered-subset expectation-maximization
PCE	Positive classification error
PET	Positron emission tomography
PHA	Pulse height analyzer
PMT	Photo multiplier tube
PRRT	Peptide receptor radionuclide therapy
ROI	Region of interest
SD	Subdivision
SPECT	Single-photon emission computed tomography
^{153}Sm	Samarium-153
STUK	Radiation and Nuclear Safety Authority (Säteilyturvakeskus)
TH	Thresholding
VoS	The number of voxels defining the sphere
^{90}Y	Yttrium-90
XCAT	Extended cardiac torso

1 INTRODUCTION

In Finland, over 11000 people die of cancer annually [1]. In 2012, worldwide there were 14 million new cases of cancer and about 8.2 million people died because of it [2]. Cancer is already the deadliest disease in the world, but it is estimated that in 2020 in Finland over 33 000 people get cancer and in 2050 worldwide about 25 million people get cancer annually [1, 2]. The amount of cancers is increasing rapidly. Partly, because of better diagnostics, but mostly because of the aging of the population and increased life expectancy [3]. New, more reliable and better medical assistance would be a great benefit in the fight against cancer. Speed and accuracy are the key words. Fortunately, the technology is developing fast, which enables new innovations also in the field of cancer treatment.

Radionuclide therapy is not a new cancer treatment technology, but the adoption of peptide receptor radionuclide therapies (PRRT) in gastroenteropancreatic neuroendocrine tumors (GEP-NETs) has revived the interest towards radionuclide therapy. Dosimetry is an important and interesting part of radionuclide therapy. The treatment dose should be big enough to cause damage to cancer cells, but sufficiently small to avoid the side effect on healthy tissue. Unfortunately dosimetry is not often performed in radionuclide therapy to tailor patient specific treatments and many times all the patients just receive the same treatment dose. This can lead to complications because the healthy tissue around the tumors gets violated during the treatment periods and the tumors might not get the required dose to produce optimal damage [4].

Dosimetry would help to identify critical organs, whose radiation dose should be kept in minimum and also to measure the dose to tumors whose radiation damage should be maximized. Tumor dosimetry partly relies on the segmentation of the tumors from the background organs. The segmentation of the tumors is necessary to get the tumor absorbed dose. This segmentation can be done manually, but it is time-consuming, subjective, error prone and not reproducible. Automatic segmentation methods on the other hand are fast, objective and often 100% reproducible [5]. Automatic methods have not been studied in PRRT before.

The main focus of this Master of Science thesis is to compare four different segmentation methods used for segmenting tumors from single photon emission computed tomography (SPECT) images used in PRRT. The segmentation methods are compared in two different parts. The first part includes segmenting with phantom data. There are six fully simulated phantoms. The phantoms model patients injected with a ^{177}Lu-dotatate radiopeptide, with a tumor in the liver. Each phantom includes one tumor and the sizes of the tumors vary between the phantoms. The second part includes segmenting with real patient data. The real patient data consists of several SPECT studies performed after three

^{177}Lu-dotatate treatments. These SPECT studies are the same studies, which have been used in actual individualized PRRT dosimetry. The aim is to find the possible differences between the segmentation methods. The comparison is done using three different methods: Dice similarity coefficient, Classification error and integral of the time activity curve. This Master of Science thesis is part of the doctoral thesis of Eero Hippeläinen, which aims to develop and validate a dosimetry software package for PRRT.

The thesis consists of five chapters, the presentation and the aim of the thesis as the first part. Chapter 2 is a literature review of the theory behind the thesis. The used material and methods are introduced in the chapter 3. The results are introduced in the fourth chapter, and they are discussed in the fifth chapter.

2 BACKGROUND

The peptide receptor radionuclide therapies are especially used for GEP-NETs. The GEP-NETs are cancers of the neuroendocrine system, and are typically diagnosed in the gastrointestinal tract, lungs, liver and/or pancreas [6]. Unfortunately, different types of GEP-NETs can be undetected for years without obvious signs or symptoms. This can cause delayed diagnosis, for which reason the cancer can be metastasized and the treatment gets more complicated. Typical symptoms depending on the source of cancer are for example diarrhea, asthma and/or heart palpations. Due to the common side effects, the GEP-NET is hard to diagnose [6, 7].

The GEP-NETs appear at all ages, the highest incidence being over 50 year old people. Typical types of GEP-NETs are for example insulinoma that makes pancreas produce too much insulin, which causes hypoglycemia, and glucagonoma, where tumor cells make pancreas produce large amounts of glucagon [6, 7].

Cancers are individual diseases; they all have their individual features (shape, mass, location, volume, aggressiveness and so on). Therefore, also the treatment processes are individual. After the cancer gets diagnosed and imaged, the next step is to decide the most suitable treatment method. Depending on the type of the cancer, the options are radiation therapy, surgery and/or medication [8]. In this thesis, the main focus is in radiation therapies and the latter two are only introduced briefly.

Depending on the aim of the treatment operation, it is either palliative or curative. A palliative operation relieves symptoms, while a curative operation cures or removes the cancer completely [3].

2.1 Surgical treatment

If the tumor is localized well and the state of the patient allows, a surgical operation to remove the whole tumor is the main treatment method. Unfortunately, in most cases the surgery alone is not the perfect solution especially, if the cancer is metastatic. Therefore, there has to be also some other treatment method(s) involved. Combination of at least two types of treatment is the standard. For example, a combination of surgery and chemotherapy. A surgical treatment treats cancer that is confined locally, while chemotherapy also kills the cancer cells that have spread to distant sites. Sometimes radiation therapy or chemotherapy is given before surgery to shrink a tumor, thereby improving the opportunity for complete surgical removal [9].

Advantages are that the surgery is relatively fast treatment method, and theoretically the whole cancer can be removed at once. Removal of the primary tumor is indicated to prevent complications such as bleeding and small bowel obstruction. Disadvantages are the possible complications and the need for patient to be hospitalized after the operation. Also, the operation can cause some physical and cosmetic harm [9].

A surgical operation can also be used for removing a tumor just partly. If tumor extension is limited or localized, then segmental resection with removal of the regional nodes is beneficiary. If the size of the tumor is large, the rest of the cancer can be treated with for example radiation therapy and/or medication. Also only metastases can be removed surgically, and the rest of the cancer with other methods [8].

2.2 Radiation therapy

Radiation therapy is divided into two main categories: external and internal radiation therapies. External beam radiotherapy focuses the radiation at the tumor from outside the body and internal radiation therapy is a form of treatment where a source of radiation is put inside the body of the patient. Approximately half of the patients diagnosed with cancer get radiation therapy during their treatment period [9] and about one third of all the cancer patients get palliative radiation therapy [3].

There are few dose quantities and terms that are important to know while working with radiation therapy and radioactive materials. These terms and their units are presented below.

Activity or radioactivity is measured by the number of atoms disintegrating per unit time. The equation:

$$A = -\frac{dN}{dt} \tag{6}$$

where dN is the total number of radioactive atoms in a given period of time dt. The minus sign means that the number of radioactive atoms decrease with time. The unit for the activity is the Becquerel.

$$\left[\frac{1}{s}\right] = [Bq]\ (Becquerel) \tag{7}$$

The activity cannot be directly converted into absorbed dose. There are several features of the ionizing radiation that has to be known first. For example, the type and the energy of the radiation. Furthermore, the effects of the ionizing radiation are different in different tissues. Thus, there are several features of the radiated object that has to be known, for example, its mass and density.

Absorbed dose is a physical quantity to measure the radiation energy absorbed by unit mass of substances. Under normal circumstances, the larger the absorbed dose, the larger will be the hazard. The absorbed dose applies to all types of ionizing radiation and substances. However, the same absorbed dose for different type of radiation under different exposure conditions can cause different biological effects on human bodies. The absorbed dose *D* is calculated with the equation:

$$D = \frac{d\varepsilon}{dm} \tag{1}$$

where the mean energy $d\varepsilon$ is imparted by ionizing radiation to matter of mass dm. [3] The unit for the absorbed dose is the Gray:

$$\left[\frac{J}{kg}\right] = [Gy]\ (Gray) \tag{2}$$

Equivalent dose measures the health effect of low levels of radiation on the human body. It takes into account the type of ionizing radiation producing the dose. It measures the biological effect of different types of radiation. The equivalent dose is calculated with the equation:

$$H_{T,R} = w_R \times D_{T,R} \tag{3}$$

where w_R is the radiation weighting factor and $D_{T,R}$ is the absorbed dose in tissue T by radiation type R. The radiation weighting factors for different types of radiation have been established by the International Commission on Radiological Protection (ICRP). The value of w_R is 1 for x-rays, gamma rays and beta particles, but higher for example for protons and neutrons. The SI unit for equivalent dose is also joule per kilogram, but the unit is the Sievert [3].

$$\left[\frac{J}{kg}\right] = [Sv]\ (Sievert) \tag{4}$$

Effective dose takes into account the absorbed doses received by different organs and tissues and weights them according to present knowledge of the sensitivity of each organ to radiation. The type of radiation is also taken into account. The effective dose is used for example for comparing the overall health effects of different radionuclides. The effective dose is calculated with the equation:

$$E = \sum_T [w_T \times H_T] \tag{5}$$

where w_T is the corresponding weighting factor established by ICRP and H_T is the equivalent dose absorbed by tissue T. The unit of the effective dose is the Sievert [10].

Sufficiently high-energetic radiation causes molecular ionization that damages cells, and eventually causes cell death. The aim is to direct the radiation straight to tumor as accurate as possible. Thus, the damage of the surrounding tissue stays low [10].

External radiation therapy is a local treatment method, so radiation does not effect on the metastases outside the radiation range. Also, most of the side effects are local. They are mostly depending on the amount of the radiation dose, treatment duration and the features of the radiated part of the body. Today, skin injuries are minor. Only minor side effects, for example redness, dryness and/or ulcers are possible. Also, mucosae can be damaged, and some ulcers and eruption can be noticed at treated areas. Also, for example diarrhea, pain, burning, tiredness and hair loss are usual. The side effects get better within next few weeks, but radiated areas will remain more sensitive than before the treatment [9].

The side effects that can be noticed months or even years after treatments are called the late side effects. The most common late side effect is extra ligament in treated areas. The extra ligament feels harder than normal tissue and can cause functional harm. One of the worst late side effects is a new cancer. Fortunately, with modern treatment systems the risk is very small, about 1-3% of the patients gets this kind of cancer during next 20-30 years after the treatment session [9].

In addition to the side effects mentioned above, radiation therapy can cause also another kind of harm for kids. Radiation causes local growth failures, hormonal imbalance and central nervous system damages. These symptoms are fortunately also rare and can mostly be avoided with modern equipment [9].

2.2.1 External radiotherapy

External radiation therapy is the most common form of radiotherapy [3]. In external radiotherapy the healthy tissue surrounding the tumor gets also some amount of radiation. It is a painless treatment method, which nevertheless can cause some of the side effects mentioned above [9].

Like a surgical operation, the external radiotherapy can be used either as a palliative or a curative treatment. A treatment time lasts minutes and the whole treatment period lasts several weeks, one treatment per weekday. The weekends are usually treatment-free. The treated patient does not have to stay in hospital during the whole period. The treatment is fractionated, so the surrounding healthy tissue gets time to recover and the side effects stay minor. Conventional fractionation dose is usually about 2 Gy per treatment time. A palliative treatment is usually given in smaller doses and shorter periods than a curative treatment [3].

The external radiation therapy is typically delivered with a linear accelerator. The patient lies on a moveable treatment table and lasers are ensuring that the patient is in the proper position. An electron gun produces electrons, that are accelerated in a wave guide. There are two possibilities to continue. The accelerated electrons can either be focused straight to the target area or be collided with a high density x-ray target, which generates the photon beam. The electron beams are useful for treating skin-deep lesions because the maximum of dose deposition occurs near the surface. The photon beams do not lose their

energy as rapidly, and thus are more useful for treating tumors located deeper inside the body [10].

With the help of a collimator the photon beam is shaped to match the wanted target area. A currently used collimator type is a multi-leaf collimator (MLC) that consists of tens of lead leaves. These leaves are individually movable, thus they can be adjusted to match the shape of the tumor, which will minimize the amount of healthy tissue being exposed to radiation [11].

There are also various different kinds of new external radiation therapy techniques. For example such methods as the CyberKnife [12] and the Gamma Knife [13]. These treatment methods can deliver radiation more accurately to the target areas from many different angles. However, the Gamma Knife is designed especially for brain tumors, and is not a useful treatment method for GEP-NETs.

The CyberKnife consists of a small linear accelerator and a moving robotic arm which allows the radiation to be directed at any part of the body from any direction. Unfortunately, a single treatment session can be long-lasting because the radiation is given from several different angles [12]. Also, its primary treatment target is a small tumor with clear lines, which GEP-NETs rarely are. In spite of new innovative methods, the external radiotherapy still is not effective enough for metastatic GEP-NETs, and the radiation dose of the healthy tissue is larger.

2.2.2 Internal radiotherapy

The term internal radiation therapy usually refers to the brachytherapy. In brachytherapy the radiation sources are close to the tumor and the radiation dose of the healthy tissue stays minor [8].

Depending on the dose rates the radioactive source is inserted to a patient by hand (with a catheter or a needle) or with a computer-controlled remote afterloading machine. When accomplishing a low dose rate (LDR) treatment the source (for example an iridium wire with the activity of 37 MBq/cm) is inserted to the patient by hand. The LDR treatment period lasts about 5-7 days, and the dose rate per treatment session is 0.4-2 Gy/h [8]. The afterloading machines are usually used with high dose rate (HDR) treatments, where the dose rate is over 12 Gy/h. The afterloading machine performs transfer, insertion and removal of the source [14].

A well-executed internal radiotherapy, either combined with external radiation therapy or alone, can produce better results than functionally extensive surgery. Other benefits of internal radiation therapy in relation to external radiation therapy are listed below:

1. Brachytherapy is faster. The treatment shortens from 4-7 weeks to 5-7 days.
2. Thus, it is also cheaper solution.
3. When the radioactive source is near the tumor, the absorbed dose of healthy tissue is much lower [14].

Brachytherapy has also some disadvantages in relation to external radiation therapy. First, the operation requires a surgical operation. Thus, it is harder to execute. This means also that there is often need for specialists. In contrast to the external radiation therapy, the patient should be hospitalized after the treatment. Also, the radiation load of the medical personnel is problematic (especially when inserting the source(s) by hand) [14].

In spite of the need of surgical treatments the complications are minor. For example infections and hemorrhage are uncommon. The other side effects are in relation to ones mentioned earlier [14].

Intracavitary brachytherapy has been used for decades to treat gynecological cancers with great results. It is also a useful treatment method for example for esophageal and nasopharyngeal cancers [14]. But like all the methods introduced above, the brachytherapy unfortunately is ineffective against metastatic GEP-NETs.

2.3 Pharmacological treatment methods

The three major modalities of the pharmacotherapy treatment are hormonal therapy, interferon therapy and chemotherapy. Pharmacological treatment methods are usually used as adjuvant treatment methods. Doses are usually taken orally or by injections. During treatment periods, the patient does not have to stay in hospital, but is able to live as normal life as it is possible with the disease [15].

In some cases, the cancer cells may be utilizing hormones produced by the body. This is prevented by certain medicines or drugs, which inhibit the production or activity of such hormones, and eventually stop the growth of the cancer or even cause cell death. The other solution is to surgically remove the endocrine organ(s) that produce(s) the particular hormone, for example the ovary, or tissue that may suffer from the hormonal activity, for example the breast tissue [16].

Interferon therapy acts as the same way as the hormonal therapy, but on the contrary, and with the difference that the acting element is interferons, proteins produced by the body. As the hormone therapy reduces the amount of hormones in the body, the interferon therapy tries to increase the amount of proteins that are fighting against the cancer cells. The main focus of hormone and interferon therapies is not necessarily killing the cancer cells but to stop the cancer cells from multiplying [17].

The most common pharmacological treatment method is chemotherapy. While traditional radiation therapy methods and surgery aim for local treating, chemotherapy is more comprehensive method and tries to cure the cancer in all over the body. The chemotherapy can be used either palliatively or curatively. However, the main use is to strenghten the effectiveness of the primary treatment methods such as radiation therapy, and relieve symptoms in cases where the patient is diagnosed with incurable cancer. [18]

Chemotherapy prevents cell division, which finally will lead to cell death and the cancer gets destroyed. Because cancer cells generally grow and divide faster than normal cells, they are more susceptible to the action of chemotherapy. However, damage to

healthy cells is unavoidable, and this damage accounts for the side effects linked to these drugs [18].

The side effects are individual depending on the doses and the used medication. Common side effects are almost similar to the side effects caused by radiation therapy treatment methods, for example tiredness, nausea, hair loss and dryness [15].

2.4 Peptide receptor radionuclide therapy

Radionuclide therapy is a form of treatment methods that is capable of treating several metastases at the same time, which is more or less difficult with the other treatment methods [19] Radionuclides have been used in medicine for decades in Finland. First in the late 1930s, radiophosphorus (^{32}P) was used in leukemia treatments and in 1954 the Finland's first radioiodide treatment was made [20].

The efficacy of treatment depends on the trapping of the radionuclide to the cancer cell by means of its carrier, and the time of retention. The whole process is quite complicated when the radionuclide follows the laws of radiation physics and radiation biology, the carrier follows the laws of pharmacology, and the compound of these two follows the laws of pharmacodynamics [20]. Basically, a radionuclide moves like a drug inside the body, but its therapeutic effect is based on the cancer cell-killing nature of radiation. Thus, radionuclide therapy cannot be clearly categorized as a form of either internal radiation therapy treatment or pharmacotherapy. In the literature, this is more or less a line drawn in water.

Most of the radionuclide therapies are performed using radionuclides, which decay by β^- decay. In β^- decay the extra neutron in the nucleus transforms into a proton, releasing negative beta radiation and a variable amount of gamma radiation [20]. The nucleus is converted into a nucleus with one higher atomic number while emitting an electron (e^-) and an electron antineutrino (ν_e). The generic equation is:

$$ {}^{A}_{Z}N \rightarrow {}^{A}_{Z+1}N + e^- + \nu_e $$

where ${}^{A}_{Z}N$ is the parent nuclide and ${}^{A}_{Z+1}N$ is the daughter nuclide. The atomic mass A stays unchanged, but the atomic number Z increases by one [10]. The emitted electron is the beta particle. Thus, the treatment effect of the radioisotopes is based on the short-ranged beta radiation. The range of beta particle is only a few millimeters depending on the energy of the emitted electrons. In addition to the beta particles the radionuclides used in radionuclide therapies often also emit gamma radiation which can be used in post-treatment imaging [21]. Gamma radiation and imaging methods are introduced later in this thesis.

Usually, the radiopharmaceutical consists of a radionuclide, its biologically active carrier and their bond, but not always. For example, radioiodide (^{131}I) does not need a carrier. The most used isotopes in radionuclide therapies are Iodide-131 (^{131}I), Yttrium-90 (^{90}Y), Lutetium-177 (^{177}Lu) and Samarium-153 (^{153}Sm). They differ in half-life, decay

energies and the amount of emitted gamma radiation [20]. ^{177}Lu, the radionuclide studied in this thesis, emits about 80% beta-radiation and about 20% gamma-radiation per decay [22].

PRRT is a relatively new treatment method. The first PRRT was made in 1996 in Switzerland. Currently, it is the most viable treatment method for GEP-NETs. PRRT is based on the use of somatostatin analogs. In GEP-NETs, the somatostatin analogs bind to somatostatin receptors. There are three radionuclides that are attached to somatostatine analogs to create radiopeptides: Indium-111 (^{111}In), ^{90}Y and ^{177}Lu of which ^{111}In is only used for imaging [21].

^{177}Lu decays by simultaneously transmitting heavily ionizing beta (β^-) radiation that destroys GEP-NETs and gamma radiation which can be imaged outside the body with a gamma camera. The binding sites can be determined with the SPECT images and that information can be used for dose calculation. The half-life of ^{177}Lu is 6.7 days and its beta particles have a range of 2 mm in soft tissue making it a good candidate for PRRT [22]. Tissue penetration is an important factor since a certain range of radiation is necessary to kill tumor cells but not damage surrounding, healthy tissues [21].

Dotatate is an amide of the acid DOTA and (Tyr^3)-octreotate, a derivative of octreotide. DOTA, 1,4,7,10-tetraazacyclododecane-1,4,7,10-tetraacetic acid, $(CH_2CH_2NCH_2CO_2H)_4$, acts as a chelator for a radionuclide. (Tyr^3)-octreotate binds to somatostatin receptors, which are found on the cell surfaces of a number of neuroendocrine tumors. Dotatate can be tagged with ^{177}Lu [21]. Structural formula of the ^{177}Lu-dotatate is presented in figure 1.

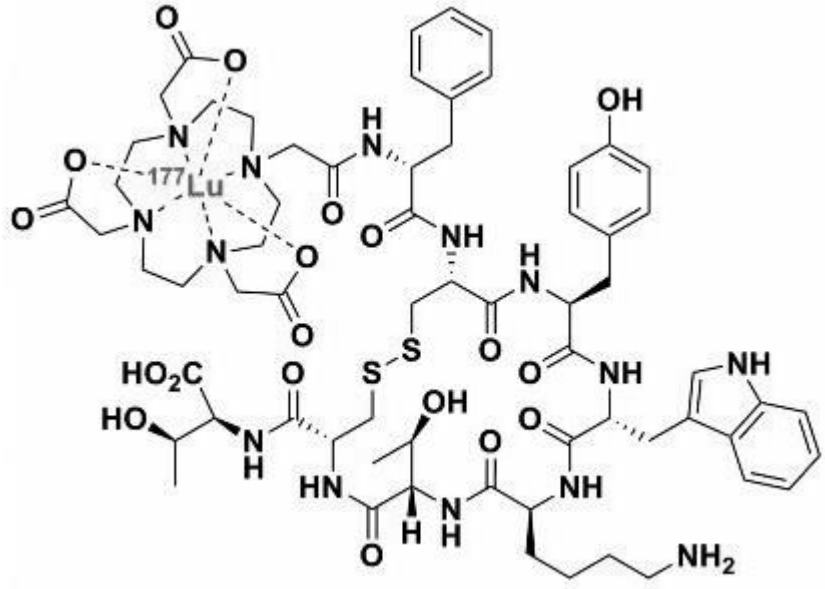

Figure 1: The structural formula of ^{177}Lu-dotatate. Adopted from [22].

Unfortunately, the somatostatin-based radiopharmaceutical does not bind only to the tumor cells, because also many normal organs express somatostatin receptors. Thus,

radionuclide therapies should be planned well so that the amount of radioactivity is maximized in tumors and minimized in critical. The treatment is performed over multiple cycles, usually administered 8-12 weeks apart. Dosing of ^{177}Lu is currently recommended at 7.4GBq/m^2 [21].

The results of ^{177}Lu-dotatate treatments have been promising. Not only the tumor sizes have been decreasing, but the total lifetime of the patient has been increasing and also the quality of life of the patients has improved. ^{177}Lu-dotatate has a particularly favorable affinity profile. Its maximum tolerated dose is limited by toxic effects especially on the kidney and bone marrow, and results seem encouraging compared with historical therapeutic data. The most common side effects of ^{177}Lu-dotatate treatments are gastrointestinal comprising abdominal pain, nausea or diarrhea that are commonly transient [21].

In spite of the promising results, the ^{177}Lu-treatments are not yet globally established. The lack of accurate dosimetry might be one of the reasons for this. ^{177}Lu-treatments are currently often based on coarse approximation of the absorbed doses and conservative dose limits for the critical organs. Randomized studies of peptide-receptor radionuclide therapy are lacking, making comparison of published data difficult [23].

2.5 Single photon emission computed tomography, SPECT

Nuclear medicine is the part of radiology in which a chemical or other substance containing a radioactive isotope is given to the patient somehow (orally, by injection or by inhalation). Once the material has distributed itself according to the physiological status of the patient, a radiation detector is used to make projection images from the x- or gamma rays emitted during radioactive decay of the agent. Nuclear medicine produces emission images, because the radioisotopes emit their energy from inside the patient [10].

SPECT-imaging is a form of nuclear imaging, which was invented in the early 1960s [24]. SPECT is a tomographic imaging method that displays two-dimensional slices of the three-dimensional spatial distribution of injected radiopharmaceutical within the patient's body. The radionuclide of the radiopharmaceutical emits gamma radiation that can pass through the body and gets detected by a gamma camera [25].

Gamma camera consists of collimator, detector crystal, photo-multiplier tubes and electronics. A block diagram of a gamma camera is presented in figure 2. Gamma radiation emitted from the injected radiopharmaceutical interacts with the body, and gets already absorbed and scattered inside the body. The gamma radiation that radiates through the patient will first collide with the collimator. The collimator is a kind of a shield in front of the scintillation crystal that blocks out unwanted photons. The basic design of a collimator is a lead plate which contains a large amount of small holes. Only the photons that travel through the holes can cause scintillations in the crystal and participate on image formation. Collimators differ by the hole diameter, hole length and the distance between hole centers. Different isotopes have different gamma energies and thus need different

type of collimators. Collimators are needed to find out the direction of the incoming radiation. [26].

Gamma rays that find their way through the collimator hit the detector crystal. The crystal absorbs gamma photons and emits light in response. The crystal is usually made of sodium iodide, NaI(Tl). The thickness of the crystal is important. It should be thick to get good sensitivity. On the other hand, it cannot be too thick. The thicker the crystal, the greater the spread of the emitted light photons produced from the scintillation. The spread affects the computation of gamma ray interaction location resulting and the resolution of the gamma camera gets poorer [26].

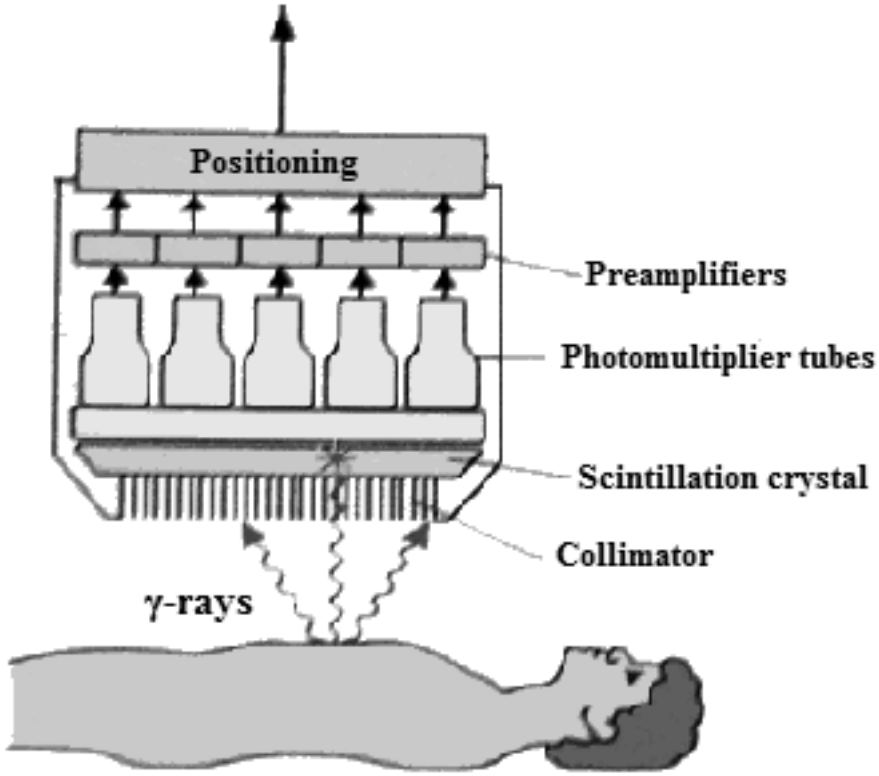

Figure 2: A block diagram of a gamma camera. Modified from [28]

Gamma photons interact with the scintillation crystal with two major methods: photoelectric absorption or Compton scattering. The photoelectric effect occurs when an incident gamma photon interacts with an inner-orbital electron and the entire energy of the gamma photon is transferred to the electron. The Compton Effect occurs when an incident gamma photon interacts with an outer-shell electron and transfers some of its energy to the electron, causing the electron to eject from its orbit. Due to the collision the energy and direction of the incident gamma photon changes. The scattered gamma photon may undergo further photoelectric absorption, or be re-scattered. With both methods, the electron raises to a higher energy level, and thus is in unstable state. As falling back to a lower energy level, the electron releases the extra energy as visible light [10].

The light emitted by the crystal is detected by photomultiplier tubes (PMTs). These tubes have two functions: convert the visible light into electrical signal and signal

amplification. The electrical signals are forwarded to preamplifiers that further amplify the signals, so as to minimize distortion and attenuation of the signal during transmission to the remainder of the system. After the preamplifiers the electrical signals is forwarded to the pulse height analyzer (PHA). The PHA is used to allow only pulses which correspond to correct gamma energy to be accepted for image formation. Finally, the electrical signal is positioned by a computer.

Gamma camera forms two-dimensional planar images, projections, where a single projection shows an in vivo distribution of the radiopharmaceutical within the body. SPECT requires that projection images are taken around the patient. These projections are reconstructed into a 3D image by reconstruction algorithms [25].

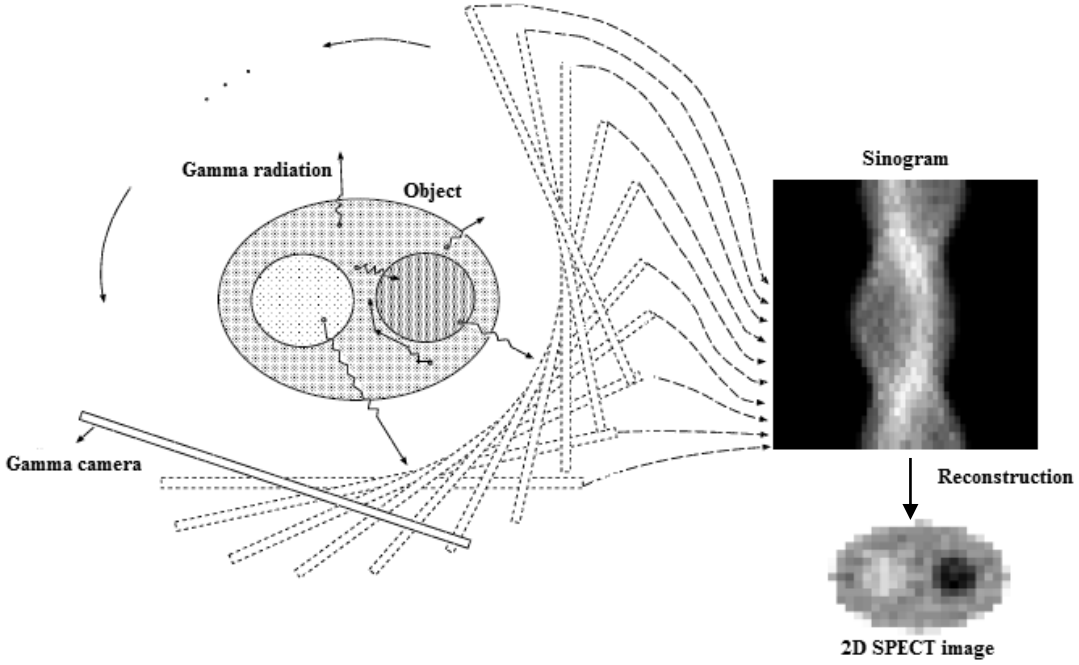

Figure 3: The basic principle of SPECT. The gamma camera rotates around the object, producing projections. The projections are combined to a sinogram, which is finally digitally reconstructed by reconstruction algorithms to a 2D SPECT image. Modified from the [25].

There are two major methods to reconstruct SPECT images, either iteratively or by filtered backprojection technique [27]. The filtered backprojection method is the most widely used analytical reconstruction algorithm due to its speed, simplicity and computational efficiency. The algorithm includes two steps: filtration of data and back projection of the filtered data. The most used iterative reconstruction method is the maximum likelihood (ML) technique. The ML technique consists of 4 steps [27] (see also figure 4):

1. Make an initial guess of the 3D image
2. Calculate 2D projections of the current 3D image estimate by forward projection

3. Compare the forward-projected projections with the actual measured projections
4. If calculated and measured projections do not match correct the 3D image and continue from 2.

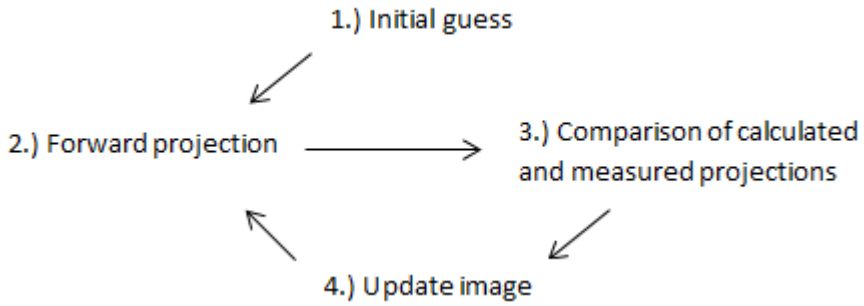

Figure 4: A diagram of the steps of the maximum likelihood technique. Modified from [43].

Modern gamma cameras are hybrid devices where gamma camera and CT scanner have been combined to form a SPECT/CT device. These devices have a lot of advantages. Of which the nearly perfect alignment of SPECT and CT images is probably the most important [10].

2.6 Dosimetry

Dose calculation is important in ensuring the safety of the radionuclide treatments. The aim is to find a proper dose to treat the cancer without causing any harm to healthy tissue. Today, dosimetry is usually performed post-treatment. All the patients receive more or less the same treatment dose, but post-treatment dosimetry can be used to check does the patient tolerate a new treatment round in the future. Dosimetry could also be used pre-treatment to tailor the treatment dose for each patient [10].

Dosimetry methods for radionuclide treatments can be roughly divided into the Medical Internal Radiation Dose (MIRD) based and voxel-based methods [10]. These are shortly described below.

2.6.1 The Medical Internal Radiation Dose, MIRD

MIRD is a mathematical tool for estimating the doses in nuclear medicine. The calculations are based on estimates or simplifying assumptions that provide approximation of the dose. The basic idea is that there are source organs and target organs. The source organ contains the radiation emitting substance, which the target organ absorbs. The mean dose to a target organ is calculated from the equation:

$$D(r_T, T_D) = \sum_{r_s} \int_0^{T_D} A(r_S, t) \frac{1}{M(r_T, t)} \sum_i E_i Y_i \phi(r_T \leftarrow r_S, E_i, t) \qquad (8)$$

where $A(r_S, t)$ is the activity for each source organ (r_S) at time (t), $M(r_T, t)$ is the target organ mass at time t, E_i is the mean energy of a given radiation emission I, Y_i is its yield (number emitted per nuclear transformation), and $\phi(r_T \leftarrow r_S, E_i, t)$ is the absorbed fraction [10].

To ease the calculation, the MIRD committee has established S factors. The S factors are estimates of the absorbed doses of organs. These S factors have been calculated with the help of phantoms that represent average human anatomy and Monte Carlo methods. For example the pancreas being a target organ and the liver being a source organ for ^{99m}Tc the S factor is 1.1 x 10^{-3} in mGy/MBq/hour. The S factor changes the equation (8) to form:

$$D(r_T, T_D) = \sum_{r_S} \tilde{A}(r_S, T_D) S(r_T \leftarrow r_S) \tag{9}$$

where $\tilde{A}(r_S, T_D)$ is the time-integrated activity (i.e. the total number of disintegrations) in source organ during the specified dose integration period T_D. According to equation (9) the only unknown quantity is the time-integrated activity in the source organs. This can be obtained by imaging the patient several times and extracting the time-activity curve from the images for each source organ. After the time activity curve has been extracted in can be easily integrated [10].

As the MIRD is based on assumptions, limitations and simplifications, there can be significant differences between the true and calculated doses. The main problems are:

1. The radioactivity is assumed to be uniformly distributed in each organ.
2. Each organ is assumed to be homogeneous in density and composition.
3. Dose contributions from minor radiation sources are ignored.
4. The organ sizes and shapes of each patient are different and might be very severly over- or underestimated by the MIRD organ sizes.
5. There is no proper dose calculation model for tumors.

Nevertheless, the MIRD is still the most commonly used dosimetry method due to its simplicity. It is primarily designed to be used in diagnostics and in radiation protection to allow direct comparison of radiation doses.

2.6.2 Voxel-based dosimetry

While the MIRD counts on average human-like phantoms, the voxel-based dosimetry uses different kind of approach to get the real anatomical and physical information about the sources and targets. Voxel-based dosimetry uses 3D dimensional SPECT or positron emission tomography (PET) images to estimate the amount of activity inside each voxel of the image and each imaging time point. These images are used as a starting point for point dose kernel or Monte Carlo calculations. In point dose kernel method a precalculated point dose kernel is used to convolve the time-wise integrated SPECT or PET image

to obtain an estimate of radiation dose in each image voxel. In Monte Carlo-based dose calculation a Monte Carlo simulator is used to track the particles and photons emitted from each source voxel and to calculate the dose to each target voxel. Both point dose kernel and Monte Carlo methods provide 3D patient specific maps of the dose in contrary to MIRD which only provides average doses per organ.

3 MATERIAL AND METHODS

This chapter covers the introduction of applied materials, software, different segmentation methods and methods for evaluating the segmentation methods. The use of these methods and materials is demonstrated at the last two subchapters.

3.1 Phantoms

Phantoms are models used for simulations, and testing, analyzing, and tuning the performance of imaging devices. Depending on the usage and the facilities, the phantom can be for example just a lead plate for testing or a complex anthropomorphic model for simulations. Today, with the modern technology the phantom can be also fully programmed. A phantom is a safer and more cost-effective solution than the use of a real human object. It also provides more consistent results than the use of a living subject or a cadaver. The biggest advantage of using programmed phantoms is that they can be easily altered to model different anatomies and medical situations, providing a large population of subjects with which to perform research [10].

As the imaging techniques started to develop, so did the phantom technology. Not until the early 1960s, the first, very simple phantoms were used to measure radioactivity doses. The organs were assumed to be homogeneous areas inside the body and the source of the radiation was assumed to be located at the center of each organ [29].

The next step was a little more complex MIRD phantom that was developed by Fisher and Snyder in the late 1960s. The doses were based on the MIRD calculations, and the phantom itself was more abundant with several different organs. As mentioned above, the MIRD simplifies the doses, and its accuracy is questionable. With these old-fashioned and so called stylized phantoms, the representation of organs is simplistic, by capturing only the most general description of the position and geometry of each organ, and thus they gave just rough estimates of the doses [29, 30].

As the imaging technology continued developing, the 3D imaging techniques such as magnetic resonance imaging (MRI) and computed tomography (CT) became popular. Hence, the new generation of 3D voxel-based phantoms was developed in the 1980s. Unlike before, the dose could be calculated based on diagnostic data, thus being more accurate than the rough estimates. Soon after this, the next step was the invention of a 4D phantom [30].

The first model of the new phantom generation was a 4D mathematical cardiac torso (MCAT) phantom. It was still based on the MIRD computational phantom, but was anatomically more accurate and realistic than the old MIRD version. Due to its geometrical design, the MCAT phantom suffered from the lack of ability to realistically model the human anatomy [29].

The next phantom model was based on imaging data, which made it much more realistic than the MCAT phantom. The non-uniform rational B-spline (NURBS) -based cardiac torso (NCAT) phantom is also used in this thesis. The NCAT phantom was originally developed for low-resolution nuclear medicine imaging research, and for that reason it includes only a limited number of structures restricted to the region of the torso. Despite or because of it, this phantom model is suitable for this thesis [29, 30].

The NURBS is a mathematical modeling tool that is widely used in computer designing, and it is very useful also with phantoms. The advantages of this method is that it can accurately represent both standard geometric objects like lines, circles and spheres, and free-form geometry like human bodies. Also, it can be evaluated relatively fast by numerically stable and accurate algorithms. The shape and volume of a NURBS -based phantom can be adjusted with coordinates of control points. This feature is useful in designing a time-dependent 4D human body modeling [29].

The phantom technology has gone even further and one of the newest versions is an extended cardiac torso (XCAT) phantom. The XCAT phantom is an updated version of the NCAT phantom. The anatomy and physiology is even more detailed, and the XCAT phantom is rather used with higher-resolution imaging applications such as MRI or CT. The accuracy of the XCAT phantom is based on the combination of NURBS and subdivision (SD) surfaces. The Subdivision surfaces are capable of modeling smooth structures with an arbitrary topological type, such as the structures in the brain. These kinds of structures are hard and almost impossible to model with the NURBS [29]. The different phantom models are presented in figure 5.

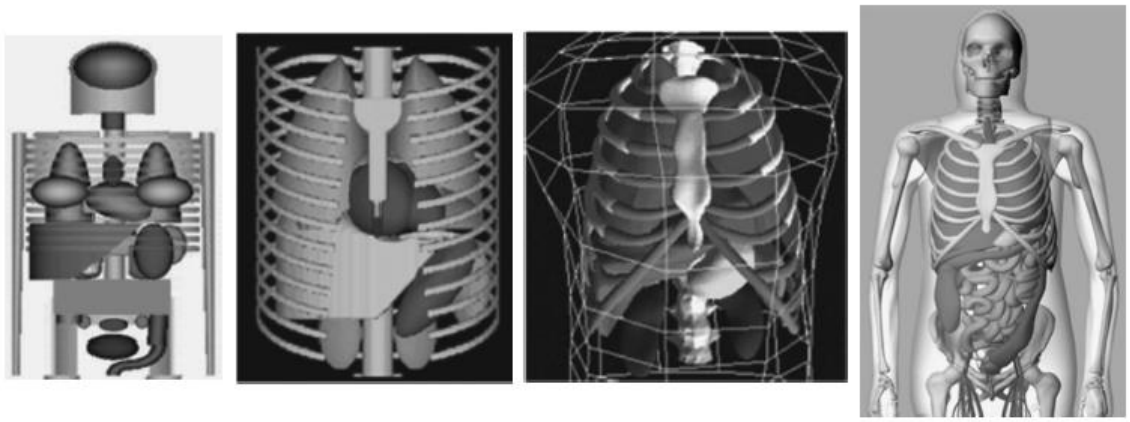

Figure 5: Different phantom models. Modified from [29].

The used phantom software can scale the phantom in many different ways (weight, height, volume), and the activities of the organs can be adjusted as wanted. The software is also able to take into account the respiratory and cardiac motions of the object.

The phantoms (6 phantoms in total) used in this study were made with default settings, only activity distributions of the organs were pre-set. The activity distributions of the organs were constructed based on 10 randomly selected anonymous patients going

through ^{177}Lu-treatment. The activity distributions were defined in two different time points: 24 hours and 168 hours after the treatment. The phantoms were created in 128x128x128-matrix size and 4.8 mm pixel size.

Lesions were included to the phantom with Matlab R2014a (The MathWorks, Inc., Natick, Massachusetts, USA), thus in practical terms the phantom is a modified NCAT phantom. The tumor sizes were 11ml, 16ml and 90ml for 24 hours, and 5ml, 15ml and 90ml for 168 hours. The idea was to have small, medium and large tumors in both groups.

After the activity and attenuation maps of the phantom had been determined, the activity projections were simulated using a Monte Carlo simulator [31]. Parameters were chosen to match the widely used Siemens Symbia SPECT/CT system. The attenuation of the radiation, the scattering in the phantom and camera characteristics were taken into account during the simulation. Images from different steps of the phantom data reconstruction process are presented in figure 6.

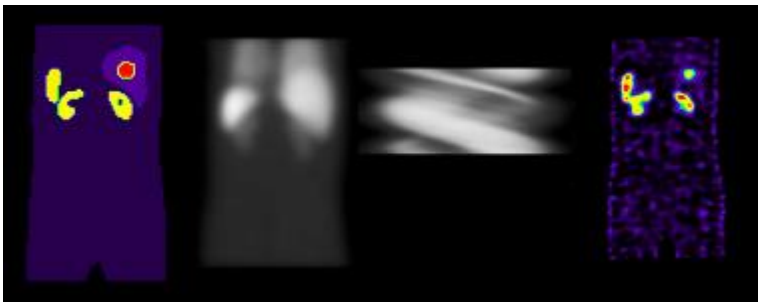

Figure 6: On the left is a coronal slice from the real phantom data. The second image from the left includes a simulated projection. The third image from the left is a sinogram from a certain height. On the right image is a coronal slice from the reconstructed phantom data.

HydridRecon reconstruction software (HERMES Medical Solutions, Stockholm, Sweden) was used to reconstruct the final slices from the projections. The used reconstruction algorithm is the ordered-subset expectation-maximization (OS-EM) algorithm. The OS-EM method is an iterative method used for mathematical optimization, and is a popular reconstruction algorithm due to its speed [32].

3.2 Segmentation methods

Image segmentation is a process, where an image is divided into multiple segments. The goal is to highlight relevant parts of the image and further improve the conditions of image analysis. Tumor dosimetry partly relies on the segmentation of the tumors from the background organs. The segmentation of the tumors is necessary to get the tumor absorbed dose. This segmentation can be done manually, but that is time consuming, subjective, error prone and not reproducible. Automatic segmentation methods on the other hand are fast, objective and often 100% reproducible [5].

Four different segmentation methods are first introduced, and then used and compared in this thesis. These segmentation methods are thresholding, k-means clustering, fuzzy-c-means clustering and expectation maximization. These methods were used to segment tumors from the SPECT images mentioned above.

3.2.1 Thresholding

Thresholding is one of the simplest, yet one of the most important and used image segmentation methods. Thresholding has several modifications, but the basic function is always more or less the same. Each voxel has its own intensity value f(x,y). The threshold value T can be chosen by the user by trial and error or with for example the help of intensity histogram of the image. When T is set, the intensity value of a voxel is compared with the threshold value T and as a result each voxel gets a new value g(x,y) as below:

$$g(x,y) = \begin{cases} f(x,y) \geq T = 1 \\ f(x,y) < T = 0 \end{cases} \tag{10}$$

A gray-scale image turns into a binary image. By changing the threshold value T, the balance of the image changes [33].

3.2.2 K-means clustering

Clustering includes a group of segmentation methods that classify objects or patterns in such a way that samples of the same group are more similar to one another than samples belonging to different groups. A clustering method tries to find a structure in a collection of unlabeled data.

The k-means (KM) clustering is a widely used segmentation method due to its simplicity. It is a method that divides an image into k different clusters and each k cluster has a centroid. The centroids are selected either manually or randomly. After the positions of the centroids have been selected, each pixel of the image is associated to the nearest centroid [5].

The second step is to calculate k new centroids as barycenters of the clusters resulting the previous step. Because of the new centroids, the pixels have to be re-associated with these new centroids [5].

After the pixels are re-associated, the balances of the clusters are changed again. The third step is to re-calculate the barycenters, and continue re-calculations step by step until the loop has found the best possible positions of the centroids. As a result the algorithm tries to minimize the following objective function:

$$J(x,c) = \sum_{i=1}^{N} \sum_{k=1}^{K} ||x_i - c_k||^2 \tag{11}$$

where *N* is the number of voxels, *K* is the number of tissue classes, x_i is a feature vector at the ith location and *c* is the kth class cluster center [5].

Noteworthy is that the k-means algorithm does not necessarily find the most optimal configuration, but the best result possible with the given k value. Unfortunately, there is no general theoretical solution to find the optimal number of clusters for any given data set. One solution is to run the algorithm several times with several different k values, and compare the results.

The KM has few disadvantages. The biggest is that each pixel can belong only to one cluster. Also, this technique is not robust to noise and spatial inhomogeneity.

3.2.3 Fuzzy-c-means clustering

Fuzzy-C-means (FCM**,** also known as fuzzy k-means) clustering is a method that tries to avoid problems that occur with k-means clustering. The FCM is developed by Dunn in the early 1970's [34] and the method is improved by Bezdek et al. in 1982 [35]. The idea is to enable a voxel to belong to more than one cluster. The algorithm works similarly to k-means algorithm, but the cluster association is done by using fuzzy membership functions developed by Zadeh [36].

The fuzzy membership function represents the amount of stochastic overlapping between the tumor region and surrounding regions. In the FCM case, the fuzzy member function at any iteration n is given by:

$$u_{ik}^{(n)} = \frac{||x_i - c_k^{(n)}||^{-2}}{\sum_{k=1}^{K} ||x_i - c_k^{(n)}||^{-2}} \tag{12}$$

and the update for cluster centers is:

$$c_k^{(n+1)} = \frac{\sum_{i=1}^{N} (u_{ik}^{(n)})^b x_i}{\sum_{i=1}^{N} (u_{ik}^{(n)})^b} \tag{13}$$

where x_i again is the feature vector at the ith location, $c_k^{(n)}$ is the kth centroid at the nth iteration and b is an exponent > 1 [5].

The algorithm follows the same steps as the k-means algorithm. First, the number of clusters have to be defined. After that, the cluster centers are updated until the algorithm finds the best position for the centroids [5].

The FCM is a popular segmentation method due to its robust characteristics for ambiguity. Also, it retains much more information than for example k-means clustering.

Nevertheless, it does not include any information about spatial context, which makes it sensitive to noise and imaging artefacts [5].

3.2.4 Expectation maximization

Expectation maximization (EM) is a stochastic modelling method that tries to exploit the statistical differences in intensity distribution between tumor and its tissue surroundings. The EM algorithm is a general approach for maximum likelihood estimation [5].

The theory behind the segmentation method is presented by Dempster et al. [37]. Each iteration of the EM algorithm involves two steps, which are called the expectation step (E-step) and the maximization step (M-step). The E-step is for computation of the probabilities and the M-step estimates the cluster parameters assuming that the intensity distribution of each class may not be Gaussian and assigns belonging probabilities according to non-Gaussian distributions [5].

The approach used in this thesis is presented by Zaidi & El Naga [5]. Zaidi & El Naga assume that the image intensities are independent and identically distributed with a Gaussian probability density function that could be divided into three regions: background, the uncertain and the target regions. The likelihood function is written as:

$$L(\pi, \mu, \sigma) = \prod_{i=1}^{N} f(x_i/\pi, \mu, \sigma) = \prod_{i=1}^{N} \sum_{k=1}^{K} \frac{\pi_k}{\sqrt{2\pi\sigma_k^2}} e^{-\frac{(x_i-\mu_k)^2}{2\sigma_k^2}} \quad (14)$$

Where N is the number of voxels, K is the number of classes, π are the mixing parameters and μ, σ are the Gaussian parameters. The maximum likelihood estimates of the unknown parameters are obtained using the EM algorithm and the probability of voxel x_i belonging to class k is given by:

$$p_{ik} = \frac{x_k f_k(x_i/\mu_k, \sigma_k)}{\sum_{m=1}^{K} \pi_m f_m (x_i/\mu_m, \sigma_m)} \quad (15)$$

The results derived using these methods will be denoted from here onwards as TH XX (XX depending on the used threshold value), KM, FCM and EM.

There is a connection between the clustering methods (FCM and KM) and the EM. The KM and the FCM could be defined as variations of the expectation maximization algorithm. Both methods even include the E- and M-steps, to be precise. In fact, the KM is also called the hard EM method in the literature, while the EM is called the soft EM method. It is a little confusing, because at the same time the FCM is called the soft version of KM, but still it is not the same thing than the soft EM method [38].

The terms *hard* and *soft* refer to the methods used for dividing the data to clusters. The KM divides the data to clusters as one data point belonging to only one cluster. This

is the *hard* method. The FCM and the EM are *softer* methods, allowing the data points to belong to several clusters [38].

The biggest difference between the clustering methods and the EM is the model of the cluster. The clustering methods model their clusters as spheres in n-dimensional space, and the EM models its clusters as probability density functions, which can have also elliptical shapes. Thus, the criterions of the segmentation are different. With clustering methods the data is clustered by the distance to a centroid, whereas the criterion for the EM-algorithm is the probability of a data point given the probability density function of the cluster center [38].

3.3 Comparison of the segmentation methods

The functionality of the segmentation methods can be seen from the images visually, but the comparison only made based on the sense of sight is subjective, and is not accurate enough or even scientifically relevant.

To get some concrete results from the data, there has to be some known comparison algorithms to use. We have three different comparison methods. Two of them, Dice similarity coefficient and Classification error are used with the phantom data. The third method, the integral of the time activity curve is used with the patient data, which was used in addition to phantom data. The patient data is described in section 3.5 in more detail.

3.3.1 Dice similarity coefficient

Dice similarity coefficient (DSC) is a spatial overlap index. It measures the similarity of two different data sets A and B. The DSC calculates the intersection of the two data sets, multiplies it by two, and divides the result with the total area of the data sets. The DSC is calculated with the given formula:

$$DSC = \frac{2(A \cap B)}{(A + B)} \tag{16}$$

Intersection formally: $A \cap B = \{x : x \in A \ \wedge x \in B\}$. The intersection is a data set that contains all elements of A that also belong to B, and vice versa, but no other elements. [39]

The DSC values range from 0, indicating no spatial overlap between two sets of binary segmentation results, to 1 indicating complete overlap. So, the closer the value is to 1, the better the result [39].

3.3.2 Classification error

The Classification error (CE) tries to find the failures the segmentation method does while segmenting the tumor from the SPECT image. It is possible that the segmentation method

classifies the data wrong either positively or negatively. The positive classification error means that the voxel is classified falsely to the sphere (lesion) and the negative classification error means that the voxel is classified falsely to the background. The CE is calculated with the formula:

$$CE = \frac{(PCE + NCE)}{VoS} \times 100\% \quad (17)$$

where PCE is the positive classification error, NCE is the negative classification error and VoS is the number of voxels defining the sphere [40, 41].

The closer the CE value is to 0%, the smaller and the better is the result of the classification error. If there is a large number of misclassified voxels, the size of classification error might get even bigger than 100%. In the literature the CE value is usually limited to 100% or 200%, since any bigger values represent complete failure of the segmentation process. In this thesis, the CE value is unlimited, because the aim is to find the differences between the segmentation methods, no matter how large the CE values are [40, 41].

3.3.3 Integral of the time activity curve

Tumor time activity curve can be generated by plotting imaging time point versus the number of total counts extracted from the SPECT images of the tumor. The integral of this curve is directly proportional to the number of decays that happen inside the tumor and therefore also directly proportional to the tumor absorbed dose, because in ^{177}Lu-treatments the locally absorbed electrons nearly create the entire dose.

The time activity curve integral was calculated by first fitting single exponential function to the raw time activity curve and then analytically integrating the exponential fitting curve from 0 to infinity. The result value is called Area under the curve (AUC).

3.4 Segmentation with the phantom data

In this part, the mathematical phantoms described in section 3.1 are under research. The lesions are segmented with four segmentation methods introduced earlier: thresholding, k-means, fuzzy-c-means and expectation maximization. Segmentation was performed using an in-house developed program ROITest. ROITest calculates the volume of the lesion, the total number of counts, and a ROI (region of interest) -mask. The software is programmed so that the ROI-mask data includes only the voxels of the segmented lesion. To get information about the functionality of the segmentation method, the resulting ROI-mask is compared with the ground truth data (i.e. the tumors extracted from the developed phantoms). At the end of the segmentation session, there are 24 different ROI-masks to

be studied and compared. The comparison with the ground truth is performed with methods introduced earlier: dice similarity coefficient and classification error. A flowchart of the phases of the work is presented in figure 7.

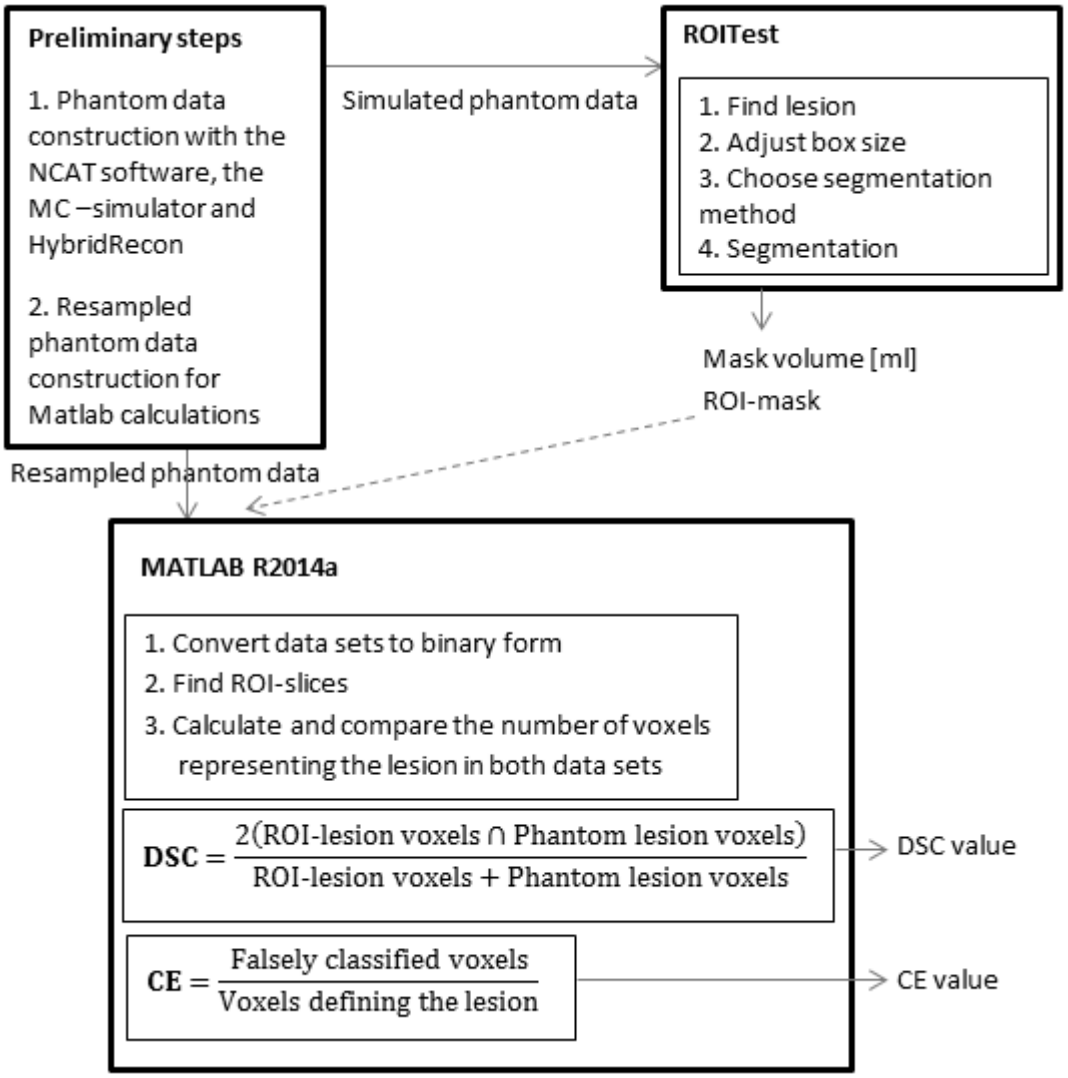

Figure 7: A flowchart of the steps of the work with the phantom data.

ROITest resamples the 128x128x128 sized phantom data and opens it as a three-dimensional, sized 256x256x256, matrix, where each layer presents a two-dimensional SPECT image. The matrix can be scrolled layer by layer as a SPECT image by a SPECT image. ROITest shows the data in three different planes: transversal, coronal and sagittal. The segmentation is implemented with the transversal images, the other two planes are just for assistance. When segmenting the lesion, the first step was to find the center of the lesion from the slices. The second step was to decide an appropriate box size, inside which the whole lesion fitted. The box size is given in centimeters. The box was used to guide the segmentation method to work on the tumor area.

The next step was to choose the wanted segmentation method and finally the software calculated the results. As a result the software generated the volume of the lesion,

the count number of the lesion, and a ROI-mask. The ROI-mask was then saved for further studies. ROITest also generates the average of the number of the counts, but it is not used in this thesis. ROITest is presented as a screenshot in figure 8.

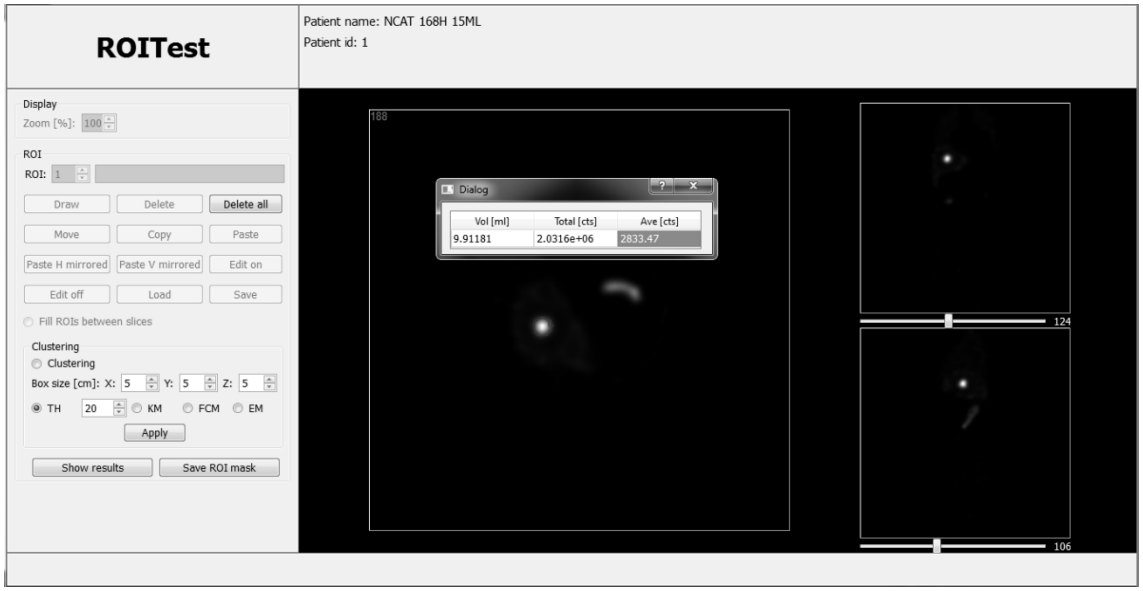

Figure 8: A screenshot of ROITest. The lesiontumor is segmented from the transversal image. The sagittal and coronal images on the left are just for assistance.

The ROI-mask was compared with the phantom data in Matlab. The used Matlab code is introduced in Appendix A. The formula (16) was used for calculating the DSC, and the formula (17) was used for calculating the CE. In DSC case, A is the ROI-mask and B is the phantom data. The comparison is first made two-dimensionally slice by slice. After that, the two-dimensional results are summed, and finally the result is a three-dimensional matrix, whereof Matlab calculates the DSC value of the whole mask. The CE comparison was made similarly first slice by slice, and finally the result comes from 3-D matrix.

3.5 Segmentation with the patient data

In this part, the same segmentation methods used with phantom data are used with real patient data. Because the real size of the lesion is unknown, there is no ground truth data available. Thus, the DSC and the CE are useless, and the integral of the time activity curve is the only comparison method used with the patient data. The lack of the ground truth data also means that the results are only estimates. The only important parameters that ROITest calculates are count numbers of the lesions.

The patient SPECT data was collected after three different ^{177}Lu-dotatate treatments. The patient was SPECT imaged after each treatment. After the first treatment the patient was imaged after 1 hour, and after 24, 48 and 168 hours. After the latter two treatments, the patient was imaged after 24, 48 and 168 hours. Hence, there is data from ten

different imaging sessions. The patient SPECT data was also reconstructed with HybridRecon. The data had several tumors, but we decided to choose just one lesion for testing the segmentation methods. The steps of the patient data segmentation have been presented in the flowchart in figure 9.

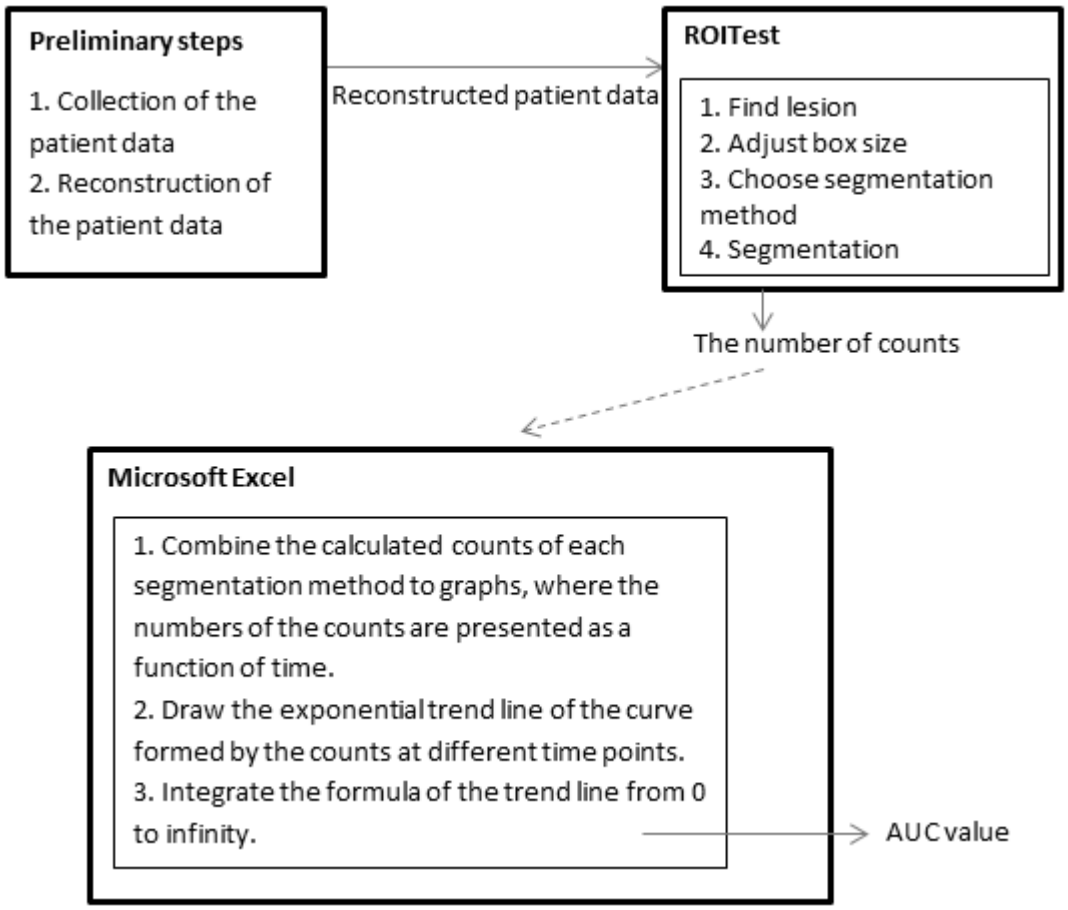

Image 9: A flowchart of the steps of the work with the phantom data.

The segmentation was again made with ROITest, and in the same way as with the phantom data. Unlike with the phantom data, there is no need for saving the ROI-masks. Just the volumes and counts are taken up. As the lesion is segmented the ROITest tells the volume and the number of counts in the segmented region. An example of the results ROITest calculated is presented in figure 10.

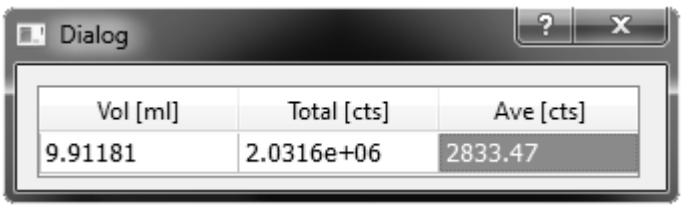

Figure 10: An example of results given by ROITest. ROITest generates the volume of the lesion, the total count number of the lesion and the average of the number of the counts.

The calculations and graphs have been made with Microsoft Excel 2013 (Microsoft Corporation, Redmond, Washington, USA). The counts calculated for each data set are combined to graphs. Every treatment has its own graph. The counts at different time points form a curve. With the help of Excel, the exponential trend line can be drawn. The value of the AUC is the integral of the formula of the trend line.

After the results were ready, it became clear that the results of the imaging one hour after the first injection were irrelevant considering the integral calculations. The trend line could have been hard to fit if the imaging data had been included to the graph. However, the data is available in the table 2. It clearly shows that the amount of the radiopharmaceutical is not yet at the maximum on the target area, one hour after the injection.

4 RESULTS

Following the procedures described in the material and methods chapter, the results of this thesis are divided into two categories: the results obtained with segmenting the phantom data and the results obtained with segmenting the patient data.

4.1 Results with the segmented phantom data

Matlab calculation of the DSC and CE values took about 36 to 38 seconds per ROI-mask. The volumes are calculated with ROITest, and their accuracy with a calculator. The results are presented in table 1. The results are listed to the table phantom by phantom. The first three are the phantoms imaged 24 hours after the treatment and the latter three are the phantoms imaged 168 hours after the treatment.

The segmentation methods are listed in relation to their accuracy, starting from the weakest accuracy. However, the last two segmentation methods listed are the thresholding values. The first one is the reference value (TH20), and the second one is the optimal value. The optimal TH values were determined by trial and error. The reference value was decided after the calculations.

The figures 11-16 are presented in the same order as the segmentation methods are in table 1 with the difference that the results with the reference value of the TH (TH20) are not imaged, but only the optimal TH values. The images are divided into six groups of four images, just like the results in the table. In the images from left to right there is the ground truth, the ROI-mask, the result with the DSC and the result with the CE. The segmentation is made three-dimensionally, but the images are pieces of the center slices of the ROIs. The three-dimensional images from the whole matrices could have been visually more aesthetic, but the needed information can be clearly seen also with the images introduced below. Furthermore, the chosen imaging style is widely used in the research literature.

Table 1: The results with the phantom data. On the first column on the left, there is information about the used phantoms. The second column from the left presents the used segmentation methods. The methods are K-means clustering (KM), Fuzzy-C-means clustering (FCM), Expectation maximization (EM) and Thresholding (TH) with a reference value and *a modified value*. The third column from the left presents the volumes calculated with ROITest in milliliters. The fourth column presents the accuracy of the calculated volume in relation to the real tumor volume presented on the first column on the left. The last two colums present the results with Dice similarity coefficient (DSC) and Classification error (CE).

Phantom data	Segmentation method	Tumor volume (ROITest) [ml]	Tumor volume accuracy [%]	DSC	CE [%]
Phantom 1	KM	7.20	64	0.73	44
Tumor volume: 11.2ml	FCM	7.30	65	0.73	43
Time from injection: 24h	EM	10.2	91	0.83	31
	TH 20	9.20	83	0.80	34
	TH 17	*10.9*	*98*	*0.84*	*31*
Phantom 2	KM	8.00	49	0.66	51
Tumor volume: 16.1ml	FCM	8.20	51	0.67	50
Time from injection: 24h	EM	13.6	84	0.84	29
	TH 20	10.8	67	0.78	36
	TH 14	*15.7*	*97*	*0.86*	*28*
Phantom 3	KM	73.5	81	0.89	21
Tumor volume: 90.2ml	FCM	72.5	80	0.88	21
Time from injection: 24h	EM	83.2	92	0.92	15
	TH 20	103.8	85	0.91	19
	TH 26	*89.9*	*100*	*0.93*	*14*
Phantom 4	KM	3.10	61	0.70	48
Tumor volume: 5.0ml	FCM	3.20	63	0.71	47
Time from injection: 168h	EM	5.10	97	0.78	44
	TH 20	4.00	79	0.75	43
	TH 15	*5.20*	*96*	*0.78*	*43*
Phantom 5	KM	7.70	53	0.67	50
Tumor volume: 14.5ml	FCM	7.70	53	0.67	50
Time from injection: 168h	EM	15.7	92	0.85	30
	TH 20	9.9	68	0.77	39
	TH 13	*14.9*	*97*	*0.85*	*29*
Phantom 6	KM	72.7	81	0.88	22
Tumor volume: 89.6ml	FCM	72.0	80	0.88	22
Time from injection: 168h	EM	87.2	97	0.93	14
	TH 20	97.8	91	0.93	15
	TH 24	*89.8*	*100*	*0.93*	*14*

The results with the imaging data of the phantom 1 with an 11ml tumor, 24 hours after the treatment are calculated with the box size of 4cm x 4cm x 4cm. The results are presented in figure 11.

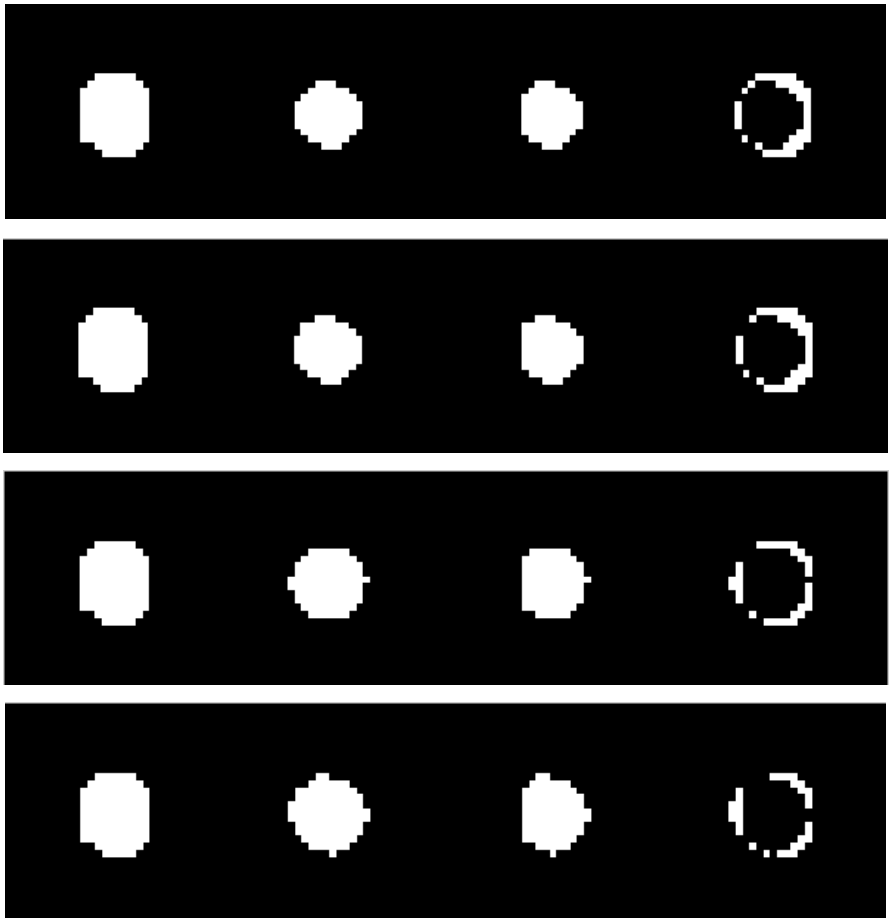

Figure 11: The result images with the imaging data of a phantom with an 11ml lesion, 24 hours after the treatment. The upper row is the results with the KM, the second row is the results with the FCM, the third row is the results with the EM and at the bottom row is the results with the optimal TH value (TH 17). The spheres are from left to right the ground truth, the ROI-mask, the result with the DSC and the result with the CE.

The results with the imaging data of the phantom 2 with a 16ml lesion, 24 hours after the treatment are calculated with the box size of 5cm x 5cm x 5cm. The results are presented in figure 12.

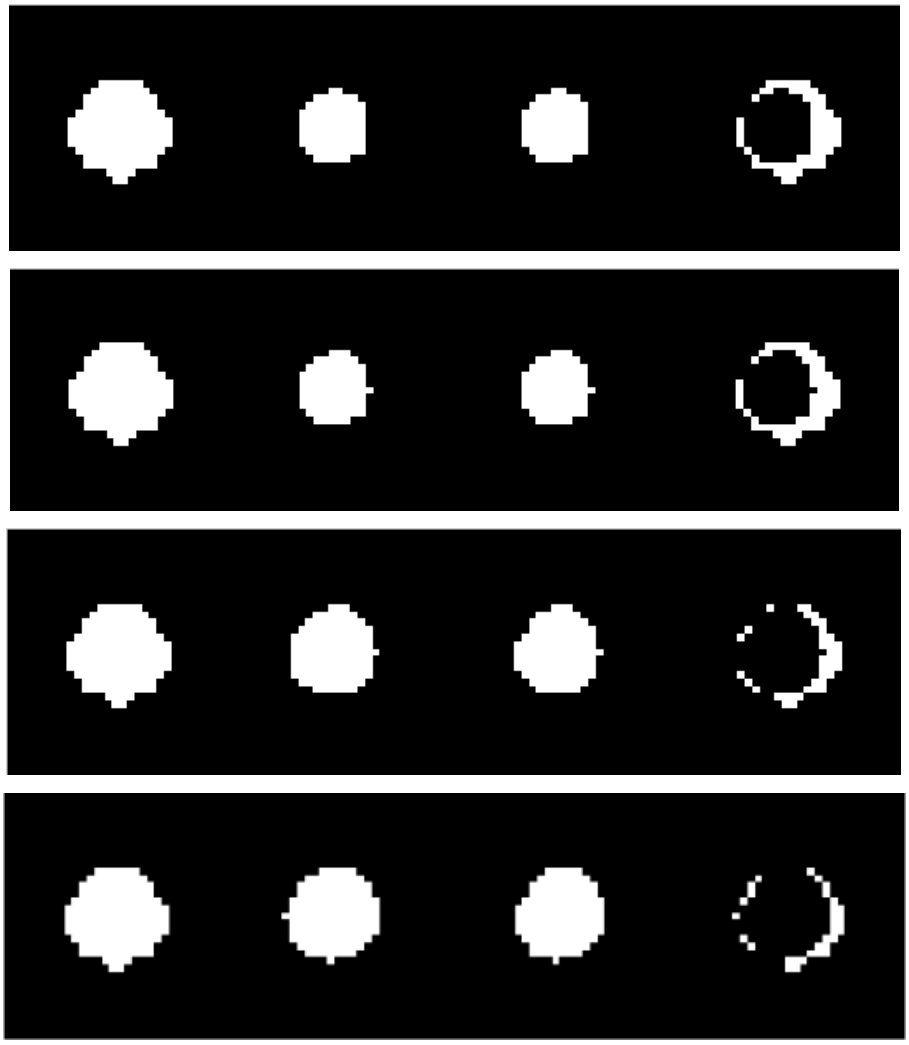

Figure 12: The result images with the imaging data of a phantom with a 16ml lesion, 24 hours after the treatment. The upper row is the results with the KM, the second row is the results with the FCM, the third row is the results with the EM and at the bottom row is the results with the optimal TH value (TH 14). The spheres are from left to right the ground truth, the ROI-mask, the result with the DSC and the result with the CE.

The results with the imaging data of the phantom 3 with a 90ml lesion, 24 hours after the treatment are calculated with the box size of 7cm x 7cm x 7cm. The results are presented in figure 13.

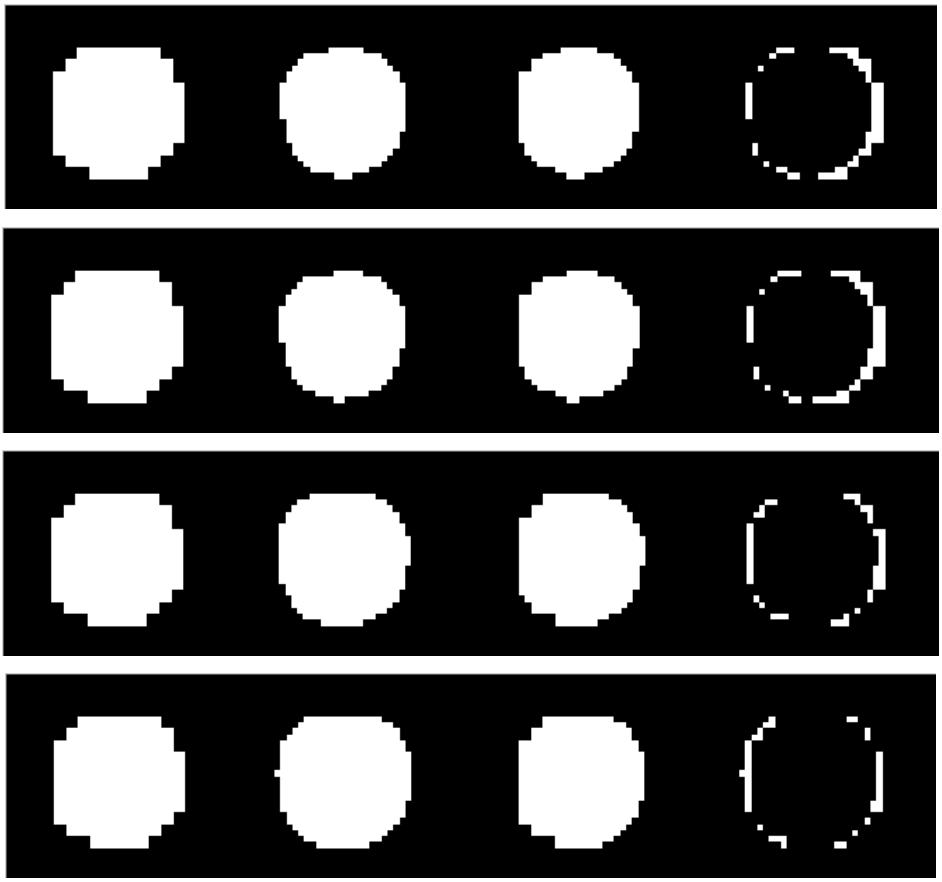

Figure 13: The result images with the imaging data of a phantom with a 90ml lesion, 24 hours after the treatment. The upper row is the results with the KM, the second row is the results with the FCM, the third row is the results with the EM and at the bottom row is the results with the optimal TH value (TH 26). The spheres are from left to right the ground truth, the ROI-mask, the result with the DSC and the result with the CE.

The results with the imaging data of the phantom 4 with a 5ml lesion, 168 hours after the treatment are calculated with the box size of 4cm x 4cm x 4cm. The results are presented in figure 14.

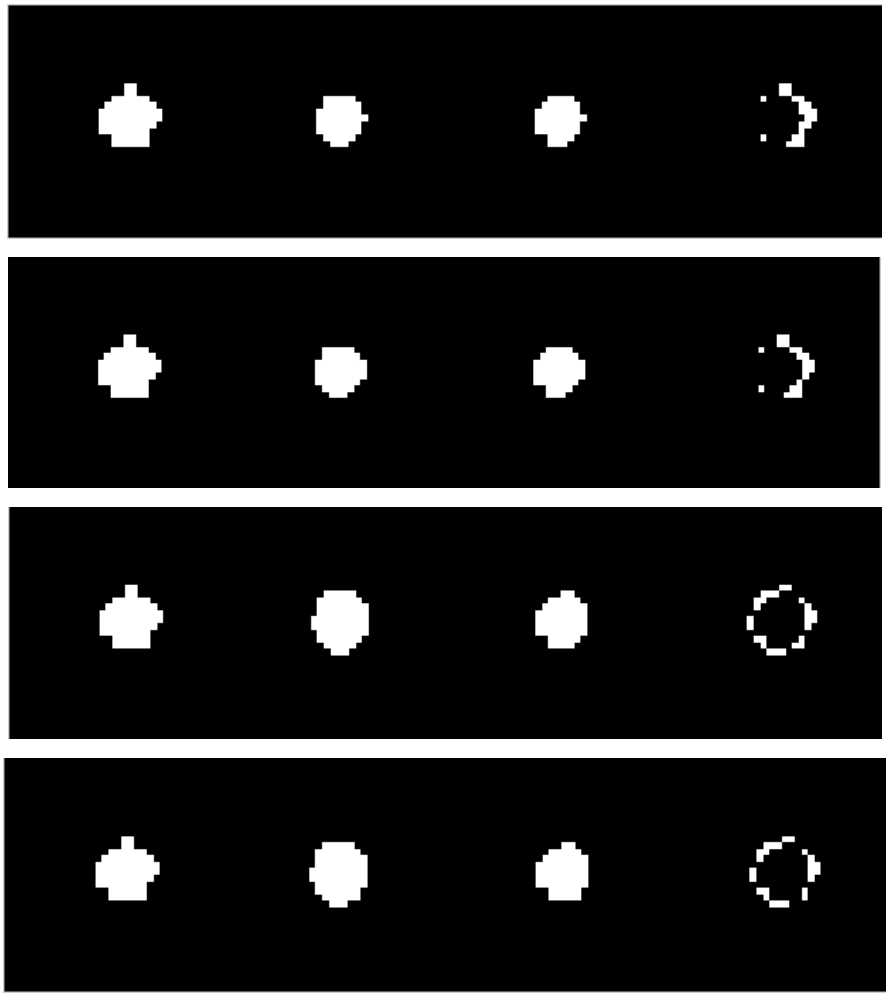

Figure 14: The result images with the imaging data of a phantom with a 5ml lesion, 168 hours after the treatment. The upper row is the results with the KM, the second row is the results with the FCM, the third row is the results with the EM and at the bottom row is the results with the optimal TH value (TH 15). The spheres are from left to right the ground truth, the ROI-mask, the result with the DSC and the result with the CE.

The results with the imaging data of the phantom 5 with a 15ml lesion, 168 hours after the treatment are calculated with the box size of 5cm x 5cm x 5cm. The results are presented in figure 15.

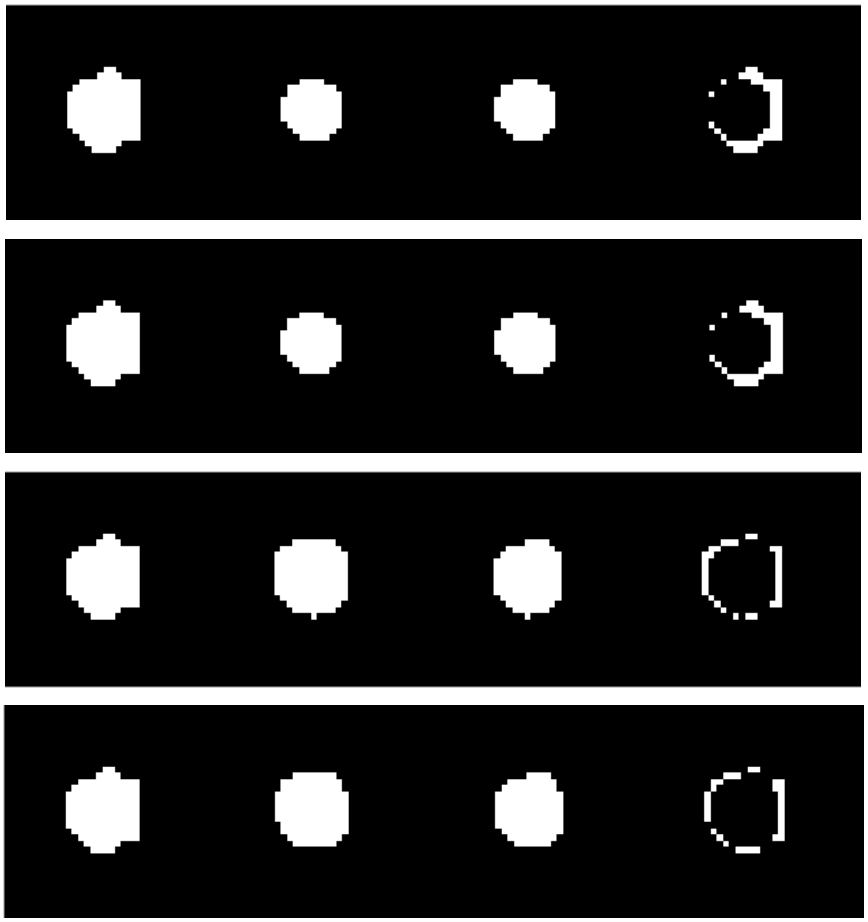

Figure 15: The result images with the imaging data of a phantom with a 15ml lesion, 168 hours after the treatment. The upper row is the results with the KM, the second row is the results with the FCM, the third row is the results with the EM and at the bottom row is the results with the optimal TH value (TH 13). The spheres are from left to right the ground truth, the ROI-mask, the result with the DSC and the result with the CE.

The results with the imaging data of the phantom 6 with a 15ml lesion, 168 hours after the treatment are calculated with the box size of 7cm x 7cm x 7cm. The results are presented in figure 16.

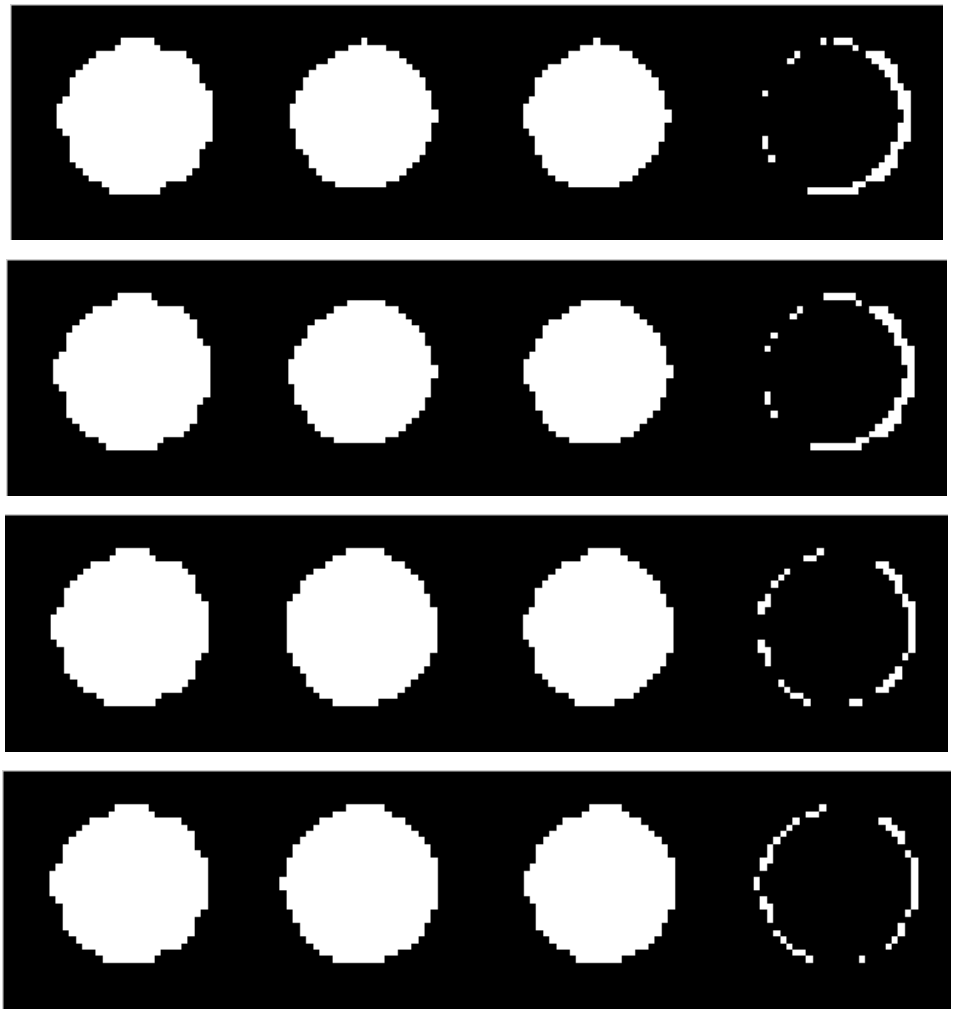

Figure 16: The result images with the imaging data of a phantom with a 90ml lesion, 168 hours after the treatment. The upper row is the results with the KM, the second row is the results with the FCM, the third row is the results with the EM and at the bottom row is the results with the optimal TH value (TH 24). The spheres are from left to right the ground truth, the ROI-mask, the result with the DSC and the result with the CE.

4.2 Results with the segmented patient data

The results are divided into three groups according to the number of the treatment. Tables 2-4 show the counts of the calculated lesion per each segmentation method per hours after the treatment. Graphs 1-3 show the same results visually.

The integral values are calculated from the curves by taking the exponential trend line of each curve and integrating them from 0 to infinity. After the integrals have been calculated the integral of different segmentation methods are scaled. The scaling is done by comparing the results to the highest integral value, the highest being 100%.

4.2.1 The first treatment

Table 2 and graph 1 include the results of the imaging period after the first treatment. Noteworthy is that table 1 includes also the count data of the imaging made one hour after the treatment. It is irrelevant information considering the AUC calculation, but it is presented here as a reference to the increasing of the counts in the target area. After a certain point the number of counts starts to decrease. The integral of the exponential fitting curve does not take into account the fact that the number of counts at time zero starts from zero, but it fits itself to the descending curve. Thus, the result is distorted.

Table 2: Results with the patient data after the first injection. On the left is the time after the treatment in hours. On the right are the counts calculated with the different segmentation methods. The factor of each count number is 10^6.

	Counts per segmentation method [10^6]			
Time [hours]	**EM**	**FCM**	**KM**	**TH 13**
1	2.2	2.1	2.1	3.2
24	3.5	2.6	2.6	3.4
48	2.8	2.0	2.0	2.6
168	1.5	1.2	1.2	1.5

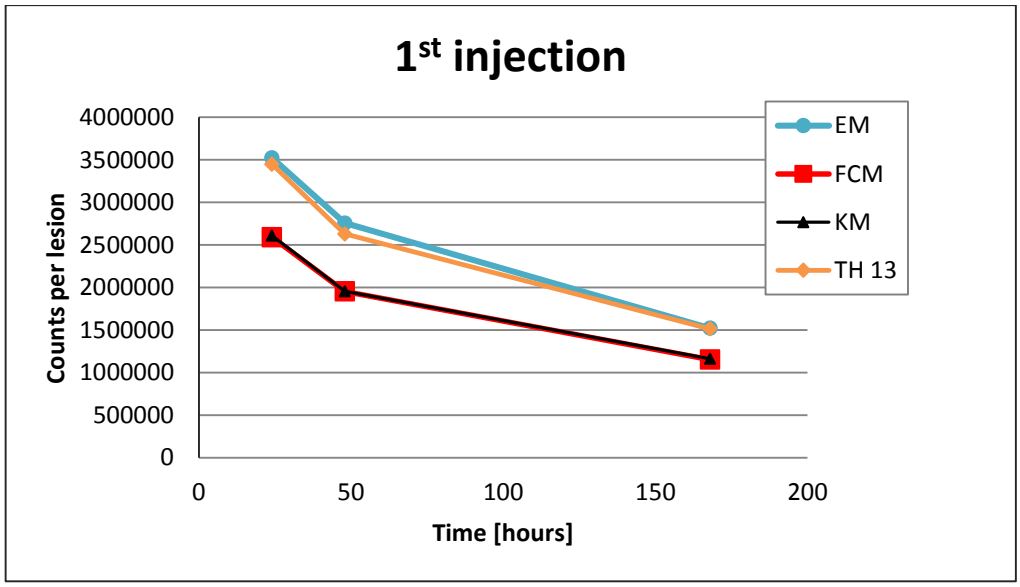

Graph 1: The results from the first treatment. The number of counts presented as a function of time.

The integrals have been calculated from the curves and the results are:

$$AUC_{EM} = \int_0^{\infty} 4 \times 10^6 \, e^{-0.006x} dx = 6.67 \times 10^8$$

$$AUC_{FCM\,/\,KM} = \int_0^{\infty} 3 \times 10^6 e^{-0.005x} dx = 6 \times 10^8$$

$$AUC_{TH} = \int_0^{\infty} 4 \times 10^6 e^{-0.005x} dx = 8 \times 10^8$$

FCM and KM has a similar curve, thus the integral is the same. AUC_{TH} has the biggest value. After scaling, the results are:

$$AUC_{TH} = 100\%$$

$$AUC_{EM} = 83\%$$

$$AUC_{FCM\,/\,KM} = 75\%$$

4.2.2 The second treatment

Table 3 and graph 2 include the results of the imaging period after the second treatment. This time, the patient is imaged only three times after the treatment.

Table 3: Results with the data after the second treatment. On the left is the time after the treatment in hours. On the right are the counts calculated with the different segmentation methods. The factor of each count number is 10^6.

	Counts per segmentation method [10^6]			
Time [hours]	**EM**	**FCM**	**KM**	**TH 10**
24	3.95	3.00	3.00	4.05
48	2.85	2.10	2.10	2.50
168	1.55	1.10	1.15	1.45

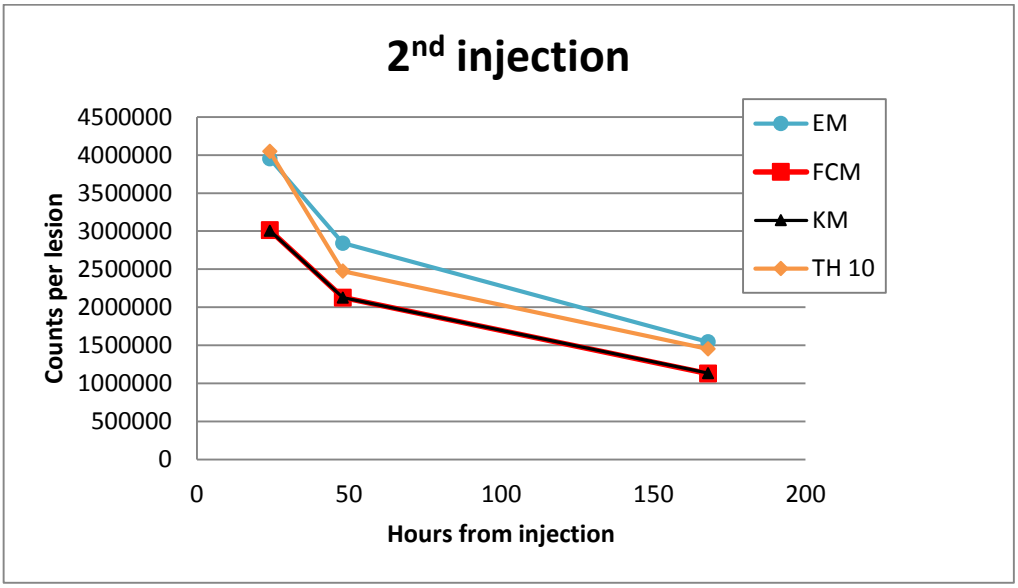

Graph 2: The results from the second injection. The number of counts presented as a function of time.

The equations of the curves are integrated, and the results are presented below:

$$AUC_{EM\,/\,TH} = \int_0^{\infty} 4 \times 10^6 e^{-0.006x} dx = 6.67 \times 10^8$$

$$AUC_{KM\,/\,FCM} = \int_0^{\infty} 3 \times 10^6 e^{-0.006x} dx = 5 \times 10^8$$

The results after scaling are presented below:

$$AUC_{EM\,/\,TH} = 100\%$$

$$AUC_{KM\,/\,FCM} = 75\%$$

4.2.3 The third treatment

Table 4 and graph 3 include the results of the imaging period after the third treatment. Noteworthy is, that the used TH value is different than the one used with the other two treatment times. This is due to the problem that with the value 10 the TH took lots of surrounding tissue or organs within, and the number of the counts was clearly miscalculated. TH 13 was the lowest value that could perform the segmentation without taking surrounding tissue within.

Table 4: Results with the data after third treatment. On the left is the time after the treatment in hours. On the right are the counts calculated with the different segmentation methods. The factor of each count number is 10^6.

	Counts per segmentation method [10^6]			
Time [hours]	**EM**	**FCM**	**KM**	**TH 13**
24	2.50	2.00	2.00	2.40
48	1.90	1.40	1.40	1.90
168	1.55	1.15	1.15	1.50

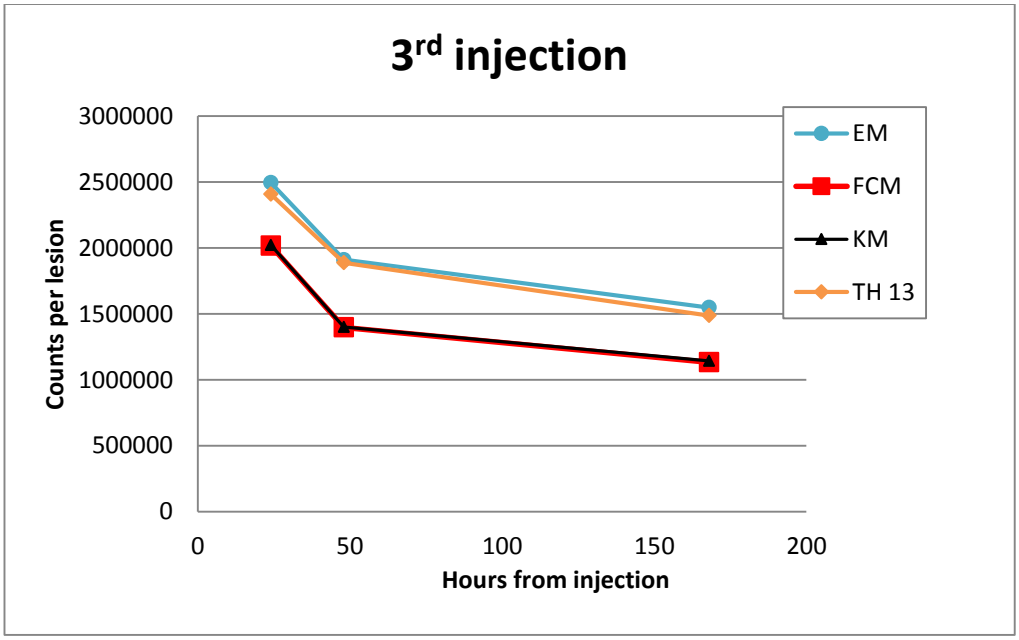

Graph 3: The results from the third injection. The number of counts presented as a function of time.

The integral of each segmentation method is similar:

$$AUC_{EM\,/\,KM\,/\,FCM\,/\,TH} = \int_0^{\infty} 2 \times 10^6 e^{-0.003x} dx = 6.67 \times 10^8$$

Thus, the result after scaling is:

$AUC_{EM\ /\ KM\ /\ FCM\ /\ TH} = 100\%$.

Noteworthy is that, as it is shown in graph 3, looks like the resulting areas would not be similar. If the areas were calculated with given points of time (24, 48,168), the areas would not match. The final result differs from the graph due to the integral of the exponential fitting curve. The integral is just an approximation of the real number of all counts from 0 to infinity. There is also a great variance between the activities. Thus, the curve fittings are hard to hit correctly.

5 DISCUSSION

The goal of this thesis was to evaluate four lesion segmentation methods (thresholding, K-means clustering, Fuzzy-C-means clustering and Expectation maximization) used in PRRT with Dice similarity coefficient, Classification error and integral of the time activity curve. The results from performed studies are interpreted in this chapter. Furthermore, the own working during the project is evaluated.

According to the phantom data results, the EM seems to be the most accurate and most reliable segmentation method of the four evaluated methods. With almost every phantom, the EM calculates the volume of the lesion with the accuracy of at least 90 percent.

Also, the results with the modified TH values are accurate, but the most optimal value changes between the volumes of the lesions and the imaging times. The results with the reference value TH20 have a great variance between different data sets.

Calculating the most optimal thresholding value with ROITest took time, because it had to be sought. In the literature, for PET images the optimal value for TH is between 40 and 50 [5, 39]. It was claimed that the TH value of 42 would be the most optimal [39, 40]. The search for the optimal TH value for SPECT images was started with those TH values presented in the literature. It was soon realized, that because the SPECT image has worse resolution than PET, the TH value has to be much lower. This research states that the optimal TH values are highly depended on the size of the lesion. With larger lesions it would be approximately 25 and with smaller about 15. As the lesion gets larger, also the TH value gets bigger. Noteworthy is, that as the TH value being the not-optimal reference value, the results still were always more accurate than with the FCM and the KM. It should also be noted that in real clinical situations optimal TH value is of course unknown.

The weakest segmentation methods are the FCM and the KM. The results with these segmentation methods are almost similar. When comparing the results, the difference between these two is really just cosmetic. The theory might give such an illusion that the FCM is a more accurate method than the KM. But when these two converge, with both segmentation methods, all the data points will be hard-assigned to a particular cluster, if the probability of it in that cluster is the highest. This denotes that the results are very close to each other.

The results are relatively more accurate with bigger (90 ml) lesions. Although, the amount of voxels is also larger, which could explain the effect. On the other hand, the results with smallest lesions (5 ml and 11 ml) are more accurate than with the medium-sized (14 ml and 16 ml) lesions.

The results are consistent and no major dispersions can be seen. Although, the results with ROITest are slightly better than the results with Matlab. For example, there are cases where the volume calculated with ROITest seems to be perfectly accurate, but

the DSC and the CE shows that there are some mismatched voxels. This tells us that the volume calculation is often not a good metric when segmentation methods are evaluated.

All the segmentation methods were sensitive to the bounding box, which is used to guide the segmentation to the tumor area, location and size. It is important to adjust it properly. If it is adjusted too large, the software includes extra material and the volume increases falsely large, and if it is too small, some parts of the tumor may stay outside the calculation.

The accuracy of the patient data results is hard to define because there is no ground truth. The results with integrating the exponential fitting curve are just rough estimates. Thus, it is not the optimal solution for evaluating the accuracy of the segmentation methods. Nevertheless, the results with the patient data are similar to the results with the phantom data. The results with the EM and the TH visually differ clearly from the results with the KM and the FCM. The patient data results also show that segmentation can have a relatively big impact on the tumor dose.

In the literature, the manual segmentation is referred to be the most accurate and widely used segmentation method there is available. It is also stated to be a time-consuming and subjective method. [5] Manual segmentation was not tested here because it requires an experienced expert to do the segmentation.

Evaluation of the own work

This work was made in co-operation with Eero Hippeläinen and Antti Sohlberg, because it is a part of Hippeläinen's doctoral thesis. The phantoms were generated, simulated, reconstructed and segmented by methods developed by Hippeläinen and Sohlberg.

My part of the work was to test the segmentation methods. I ran all the segmentation experiments and wrote the Matlab codes to analyze the results. I also wrote the thesis. There were few mistakes. Some minor, some little bigger. The most important thing is that during the practical part I was able to find my own mistakes by myself.

The generation of the Matlab codes was the most difficult and time-consuming part of the thesis, but after trial and error I managed to get the codes implemented. The early results even lead to partial rewrite of the segmentation methods, because we noticed that the segmentation works better with bigger matrix sizes.

The algorithms of the segmentation methods do not take the spatial distribution of the voxels into account. Thus, the segmented area can spread or fragment, making the region of interest distorted.

The evaluation of segmentation methods gave important information about the behavior of the four selected segmentation methods. The work brought out some problematic points, but also promising results of usability of the segmentation methods.

In conclusion, with proper settings the automated segmentation is a valuable tool for searching the regions of interest. Presumably, the quality of the automated segmentation will improve in the future with faster and more accurate software technology.

REFERENCES

[1] Cancer statistics. Finnish Cancer Registry, Institute for Statistical and Epidemiological Cancer Research. [WWW]. [Accessed on 8.10.2014]. Available: http://www.cancer.fi/syoparekisteri/en/statistics/cancer-statistics/koko-maa/

[2] Cancer. World Health Organzation. [WWW]. [Accessed on 8.10.2014]. Available: http://www.who.int/cancer/en/

[3] Jussila, A-L., Kangas, A. & Haltamo, M. 2010. Sädehoito. WSOYpro Oy Helsinki.

[4] Soimakallio, S., Kivisaari, L., Manninen, H., Svedström, E. & Tervonen, O. 2005. Radiologia. 1. painos. Porvoo. WSOY. 720 p.

[5] Zaidi, H. & El Naqa, I. 2010. PET-guided delineation of radiation therapy treatment volumes: a survey of image segmentation techniques. Springer-Verlag.

[6] Modlin, I.M., Oberg, K., Chung, D.C., JensenR.T., de Herder, W.W., Thakker, R.V., Caplin, M., Delle Fave, G., Kaltsas, G.A., Krenning, E.P., Moss, S.F., Nilsson, O. Rindi, G., Salazar, R. Ruszniewski, P. & Sundin, A. 2008. Gatroenteropancreatic neuroendocrine tumours. Lancet Oncology, 9. pp. 61-72.

[7] Öberg, K., Knigge, U., Kwekkeboom, D. & Perren, A. 2012 Neruoendocrine gastro-entero-pancreatic tumors: ESMO Clinical Practice Guidelines for diagnosis, treatment and follow-up. Annals of Oncology 23. pp. 124-130.

[8] Joensuu, H., Kouri, M., Ojala, A., Tenhunen, M. & Teppo, L. 2002. Kliininen sädehoito. Duodecim. 386 p.

[9] Johansson, R. 2012. Sädehoito. Lääkärikirja Duodecim. Kustannus Oy Duodecim.

[10] Bushberg, J.T., Seibert, J.A., Leidholdt, Jr., E.M. & Boone, J.M. 2012. The Essential Physics of Medical Imaging. Lippincott Williams & Wilkins. 1030p.

[11] Galvin, J.M., Smith, A.R. & Lally, B. 1992. Characterization of multileaf collimator system. International Journal of Radiation Oncology. Vol. 25. pp. 181-192.

[12] Mikä CyberKnife on? Kuopio University Hospital [WWW]. [Accessed 8.10.2014]. Available: http://www.cyberknifecenter.fi/mika_cyberknife_on

[13] Wu, A., Lindner, G., Maitz, A.H., Kalend, A.M.m Lunsford, L.D., Flickinger, J.C. & Bloomer, W.D. 1990. Physics of gamma knife approach on convergent beams in stereotactic radiosurgery. International Journal of Radiation Pncology vol. 8. pp. 941-949.

[14] Kumpulainen, E., Lahtinen, T. & Johansson, R.. 1996. Kudoksen- ja ontelonsisäinen sädehoito**.** Duodecim. 112(18):1710.

[15] Lääkehoito. Syöpäinfo. Pfizer. [WWW]. [Accessed on 13.10.2014]. Available: http://www.syopainfo.fi/syovan-hoito/laakehoito.html

[16] Hormonihoito. Cancer Society of Finland. [WWW]. [Accessed on 13.10.2014]. Available: http://www.cancer.fi/tietoasyovasta/hoidot/hormonihoito/

[17] Interferonihoito. Cancer Society of Finland. [WWW]. [Accessed on 13.10.2014]. Available: http://www.cancer.fi/tietoasyovasta/hoidot/interferonihoito/

[18] Solunsalpaajat. Cancer Society of Finland. [WWW]. [Accessed on 13.10.2014]. Available: http://www.cancer.fi/tietoasyovasta/hoidot/solunsalpaajat/

[19] Kwekkeboom, D.J., de Herder, W.W., van Eijck, C.H.J., Kam, B.L., van Essen, M., Teunissen, J.M. & Krenning, E.P. 2010. Peptide Receptor Radionuclide Therapy in Patients With Gastroenteropancreatic Neuroendocrine Tumors. Seminar in Nuclear Medicine. Vol. 40. pp. 78-88.

[20] Mäenpää, H. & Tenhunen, M. 2012. Syövän radionuklidihoidot - mitä uutta? Duodecim. Vol. 128. pp. 2209-2216.

[21] Practical Guidance on Peptide Receptor Radionuclide Therapy (PRRNT) for Neuroendocrine Tumours. 2011. IAEA. 114p. [WWW]. [Accessed on 13.10.2014]. Available: http://nucleus.iaea.org/HHW/NuclearMedicine/Radioguided_Surgery_and_Radionuclide_Therapy/RadionuclideTherapy/NeuroendocrineTumoursAndOtherTherapies/IAEA_Publications/PracticalGuidance/index.html

[22] Therapeutic radiopharmaceutical [177Lu] - DOTATATE. [WWW]. [Accessed on 13.10.2014]. Available: http://www.asto.gov.au/AboutANSTO/News/AC-S0-16995.

[25] Kulkarni, S. 2009. Image Quality in MAP SPECT Reconstructions. Dissertation. Stony Brook University. 217 p.

[26] Holly, T.A., Abbott, B.G., Al-Mallah, M., Calnon, D.A., Cohen, M.C., DiFilippo, F.P., Ficaro, E.P., Freeman, M.R., Hendel, R.C., Jain, D., Leonard, S.M., Nichols, K.J., Polk, D.M. & Soman, P. 2010 Single photon-emission computed tomography. ASNC Imaging Guidelines for Nuclear Cardiology Procedures. Journal of Nuclear Cardiology. pp. 941-973.

[27] Lyra, M. & Ploussi, A. 2011. Filtering in SPECT Image Reconstruction. International Journal of Biomedical Imaging. Volume 2011. 14 p.

[28] Short, N.M. The Remote sensing tutorial. [WWW]. [Accessed on 13.10.2014]. Available: http://wtlab.iis.u-tokyo.ac.jp/~wataru/lecture/rst/Intro/Part2_26d.html

[29] Segars, W.P. & Tsui, B.M.W. 2011. The MCAT, NCAT, XCAT, and MOBY Computational Human and Mouse Phantoms, Handbook of Anatomical Model for Radiation Dosimetry. Taylor and Francis Group.

[30] Segars, W.P. & Tsui, B.M.W. 2009. MCAT to XCAT: The Evolution of 4-D Computerized Phantoms for Imaging Research. IEEE.

[31] Sohlberg, A.O. & Kajaste M.T. 2012. Fast Monte Carlo-simulator with full collimator and detector response modelling for SPECT. Annals of Nuclear Medicine 26. pp. 92-98.

[32] Bryant, P.P. 2002. Analytic and Iterative Reconstruction Algorithms in SECT. Journal of Nuclear Medicine 43. pp. 1343-1358.

[33] Ferrari, S. 2011. Image segmentation. Course material for course Image Processing I. The University of Milan.

[34] Dunn, J.C. 1973. A Fuzzy Relative of the ISODATA Process and Its Use in Detecting Compact, Well-Separated Clusters. Journal of Cybernetics. Vol. 3. pp. 32-57.

[35] Bezdek, J.C., Ehrlich, R. & Full, W. 1982. FCM: The Fuzzy C-Means Clustering Algorithm. Computers & Geoscienses. Vol. 10. No. 2-3. pp. 191-203.

[36] Zadeh, L.A. 1965. Fuzzy Sets*. Information and Control 8. pp. 338-353.

[37] Dempster, A.P., Laird, N.M. & Rubin, D.B. 1976. Maximum Likelihood from Incomplete Data via the EM Algorithm. Journal of the Royal Statistical Society. Series B. Vol. 39. No. 1. pp. 1-38.

[38] Narayan, E., Birla, Y. & Tak, G.K. 2012. Enhancement of Fuzzy_C-Means Clustering using EM algorithm. International Journal of Computer Applications. Vol. 43. No. 13. pp. 43-46.

[39] Shepherd, T., Teräs, M., Beichel, R.R., Boellaard, R., Bruynooghe, M., Dicken, V., Goodling, M.J., Julyan, P.J., Lee, J.A., Lefèvre, S., Mix, M., Naranjo, V., Wu, X., Zaidi, H., Zeng, Z. & Minn, H. 2012. Comparative Study With New Accuracy Metrics for Target Volume Contouring in PET Image Guided Radiation Therapy. IEEE Transactions on Medical Imaging, vol. 31, no. 11.

[40] Hatt, M., Cheze, C., Turzo, A., Roux, C. & Visvikis, D. 2009. A Fuzzy Locally Adaptive Bayesian Segmentation Approach for Volume Determination in PET. IEEE Transactions on Medical Imaging, vol. 28, no. 6.

[41] Hatt, M., Lamare, F., Boussion, N., Turzo, A., Collet, C., Salzenstein, F., Roux, C., Jarritt, P., Carson, K., Cheze-Le Rest, C. & Visvikis, D. 2007. Fuzzy hidden Markov chains segmentation for volume determination and quantitation in PET. IOP Publishing Ltd.

[42] Macey, J.D., Williams, L.E., Breitz, H.B., Johnson, T.K. & Zanzonico, P.B. 2001. A Primer for Radioimmunotherapy and Radionuclide Therapy. American Association of Physicists in Medicine, report no. 71. Medical Physics Publishing. 82 p.

[43] Sohlberg, A.O. Quantitative SPECT. Lecture slides. HERMES Medical Solutions. 19 p.

APPENDIX A: THE MATLAB CODE

```
n=256;
pix_size=0.24;
vol=15; %REMEMBER TO CHANGE! Must match with the volume of the tumor

% Read the ROI-mask:
fid1=fopen('C:\roiTest3\mask_15ML_168H_TH20.roi');
mask=zeros(n,n,n);
for i=1:n
 mask(:,:,i)=fread(fid1,[n n],'ushort');
end
fclose(fid1);

% Read the phantom corresponding to the ROI-mask:
fid2=fopen('C:\roiTest3\ncat_168h_15ml_256.map');
phantom=zeros(n,n,n);
for i=1:n
 phantom(:,:,i)=fread(fid2,[n n],'ushort');
end
fclose(fid2);

% The tumor is the maxmimum value of the
max_val=-1/eps;
for k=1:n
  for j=1:n
    for i=1:n
      if (phantom(i,j,k)>max_val)
        max_val=phantom(i,j,k);
      end
    end
  end
end

% The phantom does not include anything else but the tumor data.
% Because the phantom has been interpolized, the tumor must be
% thresholded a little to get the proper volume.
% --
% The optimal threshold can be found with the help of the volume
% adjusted at the beginning of the script.
t_best=-1; %optimi-threshold
vol_err_best=1/eps;
for t=100:-1:1
  curr_vol=0;
  for k=1:n
    for j=1:n
      for i=1:n
        if (phantom(i,j,k)>(t/100)*max_val)
          curr_vol=curr_vol+pix_size*pix_size*pix_size;
        end
      end
    end
  end
  if (abs(curr_vol-vol)<vol_err_best)
    vol_err_best=abs(curr_vol-vol);
```

```
    t_best=t;
  end
end

% Segmentation of the tumor with the optimal threshold value:
phantom_tumor=zeros(n,n,n);
for k=1:n
  for j=1:n
    for i=1:n
      if (phantom(i,j,k)>(t_best/100)*max_val)
        phantom_tumor(i,j,k)=1;
      end
    end
  end
end

% Find the ROI-slices:
for g = 1:length(phantom_tumor(:,:,:))

    slices = find(phantom_tumor(:,:,g) == 1);
    if size(slices) ~= 0;
      slice_numbers(g) = g;
    end

end

ROI_slices = find(slice_numbers);

% ------------------------------------------------
% DSC part
pic_info_dsc = zeros(n,n,n);
for D = 1:length(ROI_slices)
% Turn mask into binary form
maskin_osa = mask(:,:,ROI_slices(D));    for m = 1:n*n;
        if maskin_osa(m) > 0
        maskin_osa(m) = 1;
        else
        maskin_osa(m) = 0;
        end
    end

fantomin_osa = phantom_tumor(:,:,ROI_slices(D));

% Intersection:
osien_leikkaus = maskin_osa + fantomin_osa;
    for f = 1:n*n;
        if maskin_osa(f) ~= fantomin_osa(f)
        osien_leikkaus(f) = 0;
        end
    end

leikkauspikselit = find(osien_leikkaus);
leikkaus_lkm = length(leikkauspikselit);
leikkaus_numero(D) = leikkaus_lkm;

maski_pikselit = find(maskin_osa);
maski_lkm = length(maski_pikselit);

fantomi_pikselit = find(fantomin_osa);
```

```
fantomi_lkm = length(fantomi_pikselit);

yhdiste_lkm = fantomi_lkm + maski_lkm;
yhdiste_numero(D) = yhdiste_lkm;

pic_info_dsc(:,:,ROI_slices(D)) = osien_leikkaus;

end

kaikki_leikkaukset = sum(leikkaus_numero);
kaikki_yhdisteet = sum(yhdiste_numero);
DSC = (2*kaikki_leikkaukset)/kaikki_yhdisteet

% ------------------------------------------------
% CE part

pic_info_ce = zeros(n,n,n);
for X = 1:length(ROI_slices)

    PCE = zeros(256,256);
    NCE = zeros(256,256);

    CE_maskin_osa = mask(:,:,ROI_slices(X));
    for q = 1:n*n;
        if CE_maskin_osa(q) > 0
        CE_maskin_osa(q) = 1;
        else
        CE_maskin_osa(q) = 0;
        end
    end

    CE_fantomin_osa = phantom_tumor(:,:,ROI_slices(X));

for s = 1:n*n
    if (CE_maskin_osa(s) ~= CE_fantomin_osa(s)) && (CE_maskin_osa(s)
    == 1)
    PCE(s) = 1;
    else if (CE_maskin_osa(s) ~= CE_fantomin_osa(s)) &&
    (CE_maskin_osa(s) == 0)
    NCE(s) = 1;
    end
    end
end

PCE_pikselit = find(PCE);
PCE_lkm = length(PCE_pikselit);
PCE_luku(X) = PCE_lkm;

NCE_pikselit = find(NCE);
NCE_lkm = length(NCE_pikselit);
NCE_luku(X) = NCE_lkm;

pic_info_ce(:,:,ROI_slices(X)) = PCE+NCE;

CE_fantomin_koko = find(CE_fantomin_osa);
VoS = length(CE_fantomin_koko);
VoS_luku(X) = VoS;
```

```
end

koko_PCE = sum(PCE_luku);
koko_NCE = sum(NCE_luku);
koko_VoS = sum(VoS_luku);

PCE_prosentit = (koko_PCE/koko_VoS)*100
NCE_prosentit = (koko_NCE/koko_VoS)*100

CE = ((koko_PCE+koko_NCE)/koko_VoS)*100

% ----------------------------------------
% Image formation:
% The position of the tumor varies between the data sets, so the
% coordinates have to be adjusted for every data set individually.
% The optimal coordinates have been already searched.
% There is a list below:
% -- 24h --
% 11ml
% middleslice = 169;
% Y = [81:111];
% X = [114:145];
% 16ml
% middleslice = 180;
% Y = [91:123];
% X = [115:144];
% 90ml
% middleslice = 188;
% Y = [92:125];
% X = [109:147];

% -- 168h --
% 5ml
% middleslice = 173;
% Y = [85:120];
% X = [115:148];
% 15ml
 middleslice = 188;
 Y = [89:123];
 X = [109:143];
% 90ml
% middleslice = 187;
% Y = [88:123];
% X = [108:143];

A = phantom_tumor(:,:,middleslice);
phantom_pic = A(Y,X);
B = mask(:,:,middleslice);
mask_pic = B(Y,X);
C = pic_info_dsc(:,:,middleslice);
DSC_pic = C(Y,X);
D = pic_info_ce(:,:,middleslice);
CE_pic = D(Y,X);

% After the proper coordinates have been adjusted, the four
% different data sets are combined into one image:
PIC = [phantom_pic mask_pic DSC_pic CE_pic];
figure, imshow(PIC);
```